Large-Scale Atomistic Simulations of Low-Energy Helium Implantation into Tungsten Single Crystals

Karl D. Hammond[a,b,*], Sophie Blondel[c], Lin Hu[d], Dimitrios Maroudas[d], Brian D. Wirth[c,e]

[a]*Department of Chemical Engineering, University of Missouri, Columbia, MO 65211 (USA)*
[b]*Nuclear Engineering Program, University of Missouri, Columbia, MO 65211 (USA)*
[c]*Department of Nuclear Engineering, University of Tennessee, Knoxville, TN 37996 (USA)*
[d]*Department of Chemical Engineering, University of Massachusetts, Amherst, MA 01003 (USA)*
[e]*Fusion and Materials for Nuclear Systems Division, Oak Ridge National Laboratory, Oak Ridge, TN 37831 (USA)*

Abstract

Large-scale molecular dynamics simulations of post-implantation helium behavior in plasma-facing tungsten single crystals reveal orientation-dependent depth profiles, surface evolution patterns, and other crystallographic and diffusion-related characteristics of helium behavior in tungsten during the first microsecond. The flux of implanted helium atoms studied, $\Gamma \approx 4 \times 10^{25}$ m^{-2} s^{-1}, is about one order of magnitude larger than that expected ITER, the experimental fusion reactor currently being constructed in France. With simulation times on the order of one microsecond, these results serve to discover of the mechanisms involved in surface evolution as well as to serve as benchmarks for coarse-grained simulations such as kinetic Monte Carlo and continuum-scale drift–reaction–diffusion cluster dynamics simulations. The findings of our large-scale simulations are significant due to diminished finite-size effects and the longer times reached (corresponding to higher fluences). Specifically, our findings are drastically different from findings published previously in the literature for (0 0 1) surfaces under a helium flux of $\Gamma \sim 10^{28}$ m^{-2} s^{-1}, which is typical of smaller size and shorter time atomistic simulations. In particular, this study highlights the atomic-scale materials processes relevant to helium entrapment and transport in metals, which have implications not only for nuclear fusion–relevant processes, but also helium-induced embrittlement in irradiated materials such as hospital equipment and fission reactor materials.

Keywords: tungsten, helium, molecular dynamics, nuclear fusion, plasma-facing material

*Corresponding author
Email address: hammondkd@missouri.edu (Karl D. Hammond)

1. Introduction

Tungsten is currently the material of choice for the divertor in magnetic-confinement nuclear fusion devices such as ITER [1] due to its high melting point and thermal conductivity, resistance to chemical erosion, and reasonably low neutron activation [2–6]. In the proposed operation of ITER and future fusion reactors, deuterium–tritium fusion is used to generate energy via the reaction [7]

$$^{2}\mathrm{H} + {}^{3}\mathrm{H} \rightarrow {}^{4}\mathrm{He}\ (3.5\ \mathrm{MeV}) + {}^{0}\mathrm{n}\ (14.1\ \mathrm{MeV}). \tag{1}$$

The 3.5 MeV helium nucleus will be swept up by the magnetic field, where it will gradually slow down until it reaches energies of 20–100 eV by the time it interacts with the surface of the divertor [3].

Helium interactions with tungsten surfaces have been found, under appropriate conditions, to generate significant changes in the tungsten surface morphology, even at energies below the threshold of physical sputtering (the value above which each helium atom has enough kinetic energy to displace a tungsten atom from the surface, sputtering it into the plasma). For tungsten, this threshold is well above 100 eV, closer to 200 eV or even 300 eV [8]. At low temperatures ($T < 900$ K, approximately) and energies in the 0–100 eV range, a non-specific damage pattern forms [9–11], resulting in potentially increased erosion or sputtering but no specific microstructure. At high temperatures ($T > 2000$ K or so), helium appears to form bubbles that burst through the surface, leaving holes on the order of 100 nm to 1 μm in diameter [12].

Intermediate conditions—ion energies greater than 20 eV and surface temperatures ranging from 900 K to 2000 K—produce what is commonly referred to as “fuzz” or “nanostructure” on the surface. This fuzz dramatically reduces optical reflectivity [13] and near-surface thermal conductivity [14] and will likely pose problems for device lifetime and related concerns in fusion devices. Fuzz was first reported in linear plasma devices [14–18], but it has since been reported in tokamaks (toroidal reactors) [19, 20] and magnetron sputtering devices [21]. It forms on various grades of tungsten, including single crystal samples [22, 23]. It occurs for pure-helium plasmas and mixed deuterium–helium plasmas [17, 24], but has not been observed for pure-deuterium plasmas. At higher ion energies, the resulting surface structure is reminiscent of coral [25, 26].

Significant efforts have been made to ascertain the mechanisms relevant to fuzz formation in helium-plasma-facing tungsten in the last eight years or so. Several research teams, includ-

ing ourselves, have performed a variety of atomistic simulations of helium interaction with tungsten over the last four to six years. These include studies of the growth of over-pressurized bubbles in both tungsten [27–30] and titanium [31]; effects of sub-surface bubbles on sputtering yields [32, 33]; helium interactions with surfaces and grain boundaries [27, 34–36]; helium bubble formation and growth, both in the bulk [37–40] and near surfaces [41], and direct or indirect implantation of helium atoms to a tungsten surface to observe dynamics and other effects [27, 42–46]. This growing body of work has strongly suggested that the initial stages of fuzz formation are due to helium bubble formation and the subsequent stress and strain associated with growing bubbles, with surface features grown by ejection of dislocation loops and/or individual Frenkel pairs that form adatoms, possibly including surface rearrangements. They also indicate that the presence of helium bubbles immediately below the surface does not strongly affect the sputtering yield [32, 33], though experimental studies have shown that sputtering is reduced by the presence of fuzz relative to fuzz-free surfaces [47].

Such short-time, high-flux studies have in turn either prompted or were coincidentally accompanied by experiments that attempted to "bridge the gap" (so to speak) from the other side: performing experiments at relatively low fluence in attempts to observe the initial stages of rudimentary fuzz growth. Ohno and coworkers [48], using NAGDIS-II [49], studied 25 eV helium incident on tungsten at 1700 K at a flux of $\Gamma = 1.4 \times 10^{23}$ m^{-2} s^{-1} and a fluence of $\Phi = 5.6 \times 10^{26}$ m^{-2} (10,800 s). They reported different surface morphologies for different surface orientations, all of which were decorated with $\sim$ 100 nm pores: {1 1 0}, smooth, parallel waves; {1 0 0}, jagged, mostly parallel waves; {2 1 1}, disordered, flat waves; {1 1 1}, interrupted patterns of surface features with tent-like appearance; {3 1 0}, craggy surface with no clear order; {2 1 0}, flat with no discernible pattern; {7 4 0}, flat with occasional blister-like growths approximately 400–500 nm across; {3 2 0}, similar to {7 4 0} except with raised linear features approximately 1 μm long and 100 nm wide in place of blisters. Parish and coworkers [50] performed a similar experiment, this one using 80 eV helium ions at a flux $\Gamma = 10^{20}$ m^{-2} s^{-1} up to a fluence $\Phi = 4 \times 10^{24}$ m^{-2} (11 h) at $T = 1400$ K, and also found that different surface orientations yielded different surface features. They observed pyramidal structures, which were more common on {1 0 0} faces; "wave" and "terrace" structures, which were characteristic of {2 1 1}, {3 1 1}, and {4 1 1} orientations; and "smooth" regions, which were associated with surfaces such as {2 0 1}, {3 0 1}, and {4 0 1}. A recent study by Donovan and coworkers [51] attempted very low-flux ($\Gamma = 2.4 \times 10^{19}$ m^{-2} s^{-1}) implantation with 47 eV helium ions for a

total fluence of $\Phi = 3.5 \times 10^{24}$ m^{-2}; they observed small (< 150 nm diameter) bubbles and pits with heights of up to 40 nm and depths of up to 15 nm. These experiments, for now, are the closest to observing the initial stages of fuzz formation.

What is missing from the experimental studies is an extremely-low-fluence example that is comparable to the results from simulations. The four to eight order-of-magnitude gap in fluence between existing experiments and simulations is unlikely to be bridged in the near future—running a plasma experiment that is on for less than a second is generally infeasible. On the computational side, nearly all of the simulation results published to date are representative of helium exposure at extremely high flux. Values of $\Gamma \sim 10^{27}$ m^{-2} s^{-1} [45], 10^{28} m^{-2} s^{-1} [27], or even 10^{29} m^{-2} s^{-1} [46] are typical—some 4–6 orders of magnitude higher in flux than in even the highest-flux plasma devices. These simulations are also susceptible to finite-size effects, such as stress fields associated with bubbles and/or bubbles themselves self-interacting or even merging across periodic boundaries [27, 44, 46, 52].

What we present here is work that seeks to eliminate some—though by no means all—of the shortcomings of previously published molecular dynamics (MD) studies of helium in tungsten by increasing the system size in both space and time. This accomplishes several goals. First, it allows us to decrease the flux without reducing the insertion rate significantly, keeping the simulations tractable (as they must be restarted every few hours in accordance with execution policies at computing facilities). Second, it reduces the self-interaction problem, as the next periodic image is now approximately 50 nm away, rather than 5–7 nm away as it is in smaller simulations. Finally, it gives a much better estimate from a statistical point of view of helium retention, the onset of bubble formation, cluster size distributions, and so on, simply because there are so many more atoms to work with. The longer times involved—the simulations themselves ran (discontinuously) for a period of two to three years—provide an important glimpse into the early stages of helium plasma exposure, with times $\sim$ 1 μs rather than times $\sim$ 1 ns or $\sim$ 10 ns, which are typical in most molecular dynamics simulations.

The result of such simulations, which we dub “large scale MD” simulations, is that we observe a very pronounced difference between different surface orientations both with respect to the nature of the surface evolution that results, as well as the relationship between growing bubbles and surface features. There is also a marked difference in helium retention between surface orientations, which stems primarily from the ease of near-surface bubble nucleation, as described in our previous work [41, 53, 54]. Near-surface bubble size distributions are,

perhaps surprisingly, very similar across different surface orientations. Size distributions far from the surface are largely independent of surface orientation, but also—surprisingly—largely independent of time for bubbles at depths below 10 nm or so.

The remainder of this article discusses the methods (Section 2) used in the simulations, then presents and discusses the results (Section 3). The "discussion" section (Section 4) delves into a more thorough discussion of these results as they relate to previously published results and to the field of plasma-facing materials, as well as specific phenomena observed in the simulations that require further explanation. Finally, we summarize our conclusions in Section 5.

2. Methods

2.1. Molecular Dynamics Simulations

Molecular dynamics simulations of structural evolution due to helium implantation in tungsten were conducted using the Large-scale Atomic/Molecular Massively Parallel Simulator (LAMMPS) [55], a classical molecular dynamics program primarily developed at Sandia National Laboratories. Tungsten–tungsten interactions in this work were described by the Embedded Atom Method (EAM) potential model of Finnis and Sinclair [56, 57] with subsequent short-range modifications by Ackland and Thetford [58] and extreme-short-range modifications by Juslin and Wirth [59]. Helium–tungsten interactions were pair-wise repulsive from the model of Juslin and Wirth [59], while helium–helium repulsions were described by the pair potential of Beck [60, 61] as modified at short range by Morishita et al. [62]. At the time these calculations began, these potential energy models were considered to be—and perhaps still are—the state of the art.

We studied four crystallographic surfaces—(0 0 1), (0 1 1), (1 1 1), and (2 1 1)—which were chosen as representative surfaces with different atomic-level arrangements. They also span the entire range of depth distributions for "flat" surfaces as studied in our previous work [53, 63].

Each simulation involved an approximately 50 nm × 50 nm slab of tungsten oriented with a particular low-index crystallographic surface facing the plasma. Each slab was approximately 21–25 nm thick, as described in greater detail below, with crystal orientation vectors corresponding to the orientation of the surface and periodic boundary conditions applied in the horizontal (non-plasma-facing) directions. The lattice parameter (values given below) was chosen separately for each surface, and was chosen so that the pressure in the box in the absence of helium—that is, prior to irradiation—was reasonably close to a pressure of $P = 0$ bar.

[Table 1 about here.]

The simulations involved direct implantation of helium atoms into the tungsten slab, rather than high-energy irradiation, using the procedure described in our prior work [53]. This is done to make the simulations tractable: without this simplification, helium atoms enter the system at very high velocity (about 70000 m/s, or 700 Å/ps), meaning a much smaller time step must be used until the helium atom slows down to thermally-consistent velocities. It takes 2000–12000 "extra" time steps for every helium insertion to allow the helium atom to slow down to the point where the time step can be restored to its nominal value of 0.5 fs without significant time integration errors, and even then, a significant fraction of those helium atoms simply scatter off the surface with no effect on the surface. We estimate that—at a minimum—40% of our computational budget would be spent simulating these small-timestep periods, and that it would take roughly 44% more time to run the simulations, even if every atom of helium were to become embedded below the surface. Since reflection rates on flat surfaces are as high as 70%, this means direct-bombardment simulations would likely spend the vast majority of our computational budget on capturing the physics behind the scattering of helium atoms off the surface, a process which will not affect the material's structural and morphological evolution.

The ramifications of the direct-implantation procedure are relatively minimal: Even at 100 eV kinetic energy, the chances of a helium atom displacing a tungsten atom far enough to form an adatom are minimal. ~~The~~ One might expect the depth profile should perhaps "shallow out" due to trapping of helium in bubbles near the surface, but this will make only a very minor difference in the depths reachable, as the median depth of helium penetration is only 1–2 nanometers for all surface orientations [53, 63]. To test this assumption and the validity of the direct-helium-implantation procedure, we prepared 3000 independent bombardments of a (0 1 1) surface after 100,000 helium insertions, which is the system at the bottom of Figure 3 (1 µs). The resulting trajectories involved 932 embedded atoms (approximately 31% of all the helium atoms that impinged on the surface) that did not reflect; of those, 289 helium atoms ended up near bubbles, though most of those were small bubbles near the maximum of the depth distribution. The resulting depth profile, shown in Figure 1, is similar to—and actually slightly *deeper* than—the distribution we used in the direct implantation procedure. The approximation would likely get worse at higher fluence, though it should be noted that at some point, near-surface bubbles will burst. The minor differences between the two depth distributions are likely due to three reasons: (1) imperfect statistical averaging, (2) trapping of

helium bubbles in near-surface clusters, and (3) features in the non-planar morphology that are not present in the initial planar surface.

[Figure 1 about here.]

Helium atoms were implanted, on the average, every 10 ps, representing a helium flux from the plasma with flux $\Gamma_{\text{nominal}} \approx 4.0 \times 10^{25}$ m^{-2} s^{-1}, ignoring reflections. The depth of implantation was sampled from a depth distribution consistent with 100 eV incident energy and varying with the surface orientation, as described in our previous work [53]. The interval between insertions was drawn from an exponential distribution, $\Delta t = -(\ln u)/\tau$, where $\tau = 10$ ps and $u \in (0, 1]$ is a pseudorandom number drawn from a uniform distribution; the random number generator [64] has a very long period and was also used to sample the depth distribution of inserted helium atoms and to choose their horizontal locations. This insertion rate corresponds to a helium flux to the surface of approximately $\Gamma_{\text{nominal}} = 4.0 \times 10^{25}$ m^{-2} s^{-1}, where the subscript "nominal" indicates the flux of *implanted* helium ions, as opposed to those that may reflect off the surface without implanting. This number may be converted to the actual flux using Equation (2),

$$\Gamma_{\text{actual}} = \frac{1}{1 - r}\Gamma_{\text{nominal}}, \tag{2}$$

where r, the reflection probability, is different for each surface orientation [53]. As such, the *actual* flux and fluence values are higher than the flux of embedded ions (the "nominal" flux, as we call it here), as in Table 1.

Each simulation supercell has at least 1.3 nm of vacuum *below* the supercell, as well as a thin layer of atoms that are fixed (not time-integrated) at their initial crystallographic coordinates throughout the simulation. This "frozen" layer prevents helium and tungsten atoms from leaving the simulation box through the bottom. This is a better approximation for tungsten than it is for helium: the frozen layer creates a more or less reflective surface for incoming helium atoms, which creates a slightly elevated population of helium atoms near the bottom of the box; these "extra" atoms would normally have diffused through the bottom of the box into the tungsten below. Some of those atoms would return to the box by back-diffusion, but the approximation must be made for tractability purposes that either *all* the atoms (helium *and* tungsten) come back into the simulation box after touching the bottom of the box, or *none* of them do. We chose the former approximation here.

The temperature was controlled to 933 K (660 °C) by a Nosé–Hoover "chain" thermostat [65–67], which (a) maintained quasi-Canonical ensemble dynamics in the non-frozen parts

of the simulation box, (b) prevented artificial cooling due to the frozen layers at the bottom, and (c) removed and/or added heat to the simulation to compensate for the inserted helium atoms. Each simulation was "balanced" across processors every 1000 helium insertions and every time the simulation was restarted so as to distribute the load more or less equally among processors. The temperature was chosen to ensure that 100 eV was still well below the sputtering threshold and so as to be near the temperature associated with the onset of fuzz formation.

2.2. Visualization

We employ the atomistic visualization tool OVITO [68] for most images that show atom-by-atom visualizations. We also employ the free visualization tool AtomEye [69] to probe surface atoms, helium atom locations, and so forth. Surface features, such as in the images on the left side of the first four figures, are made in OVITO by color-coding the atoms according to their z-coordinates, with atoms 0 nm above the original surface being black and those 1 nm above the surface being white; adatoms in between shaded in grayscale, proportional to their height.

2.3. Bubble Growth (V/He Ratio) Analysis

Plots of helium bubble growth (evolution of helium to vacancy ratio with time as an implicit parameter) are made via post-processing of MD simulation data by something akin to the following procedure.

1. Assign helium atoms to clusters—groups in which all atoms are closer than a particular cutoff distance, r_{He}, from at least one other atom in the same cluster. We used a cutoff of $r_{\mathrm{He}} = 1.05a$, corresponding to slightly greater than one W–W second-nearest-neighbor distance (which is a, on the average). This step determines the number of helium atoms in each cluster/bubble.
2. Find the center of mass of each helium cluster.
3. Delete all helium atoms (this step could be modified if retaining the helium atoms is desired, as would be the case in a running simulation not analyzed by post-processing methods).
4. Create new helium atoms (or another unused atom type) on a lattice consistent with the positions of tungsten atoms before any helium was added.

5. Delete all newly-created atoms that overlap by more than a certain cutoff distance, r_V, with any tungsten atoms. We used $r_V = 0.61a$, which is significantly larger than any thermal fluctuations and therefore unlikely to cause false positives or false negatives.
6. Arrange the newly-created atoms into clusters, just as with the helium atoms, with a cutoff distance $r_B = 1.05a$. We shall subsequently call clusters of such newly-created atoms "bubbles." This cutoff distance was chosen to be equal to the helium cutoff, so as to ensure that any bubbles would be more likely to be identified consistently—otherwise, the algorithm would frequently identify one bubble but two helium clusters, or vice-versa. This step determines the number of vacancies in each bubble.
7. Find the mean position of each bubble.
8. Find the closest helium cluster to each bubble, using the minimum-image convention across all periodic directions. The bubble is considered to be a void (filled with vacuum) if the closest helium cluster is more than $1.25a$ away, which corresponds to partway between the second- and third-nearest-neighbor W–W distance.

The various cutoff distances chosen are based on the idea that helium atoms are "clustered" if they are closer than second-nearest-neighbor tungsten atoms in the body-centered cubic lattice. There were no pre-existing vacancies in the simulations, so we can be reasonably assured that all vacancies are formed by helium-induced trap mutation and/or bubble nucleation. We originally chose a shorter helium cutoff distance, but doing so resulted in numerous helium clusters being mis-identified by the algorithm as being detached from vacancies due to small differences in the center of mass between the helium atoms and the vacancy clusters that resulted when they were removed.

The bubbles from each snapshot in time were tracked based on the observation that a helium cluster larger than 6–7 helium atoms will instantaneously nucleate a single-vacancy helium bubble [27]. As such, clusters of eight or more helium atoms are always associated with one or more vacancies, and will therefore not move significantly over MD-relevant time scales. Two bubbles from different snapshots are assumed to represent the same bubble if the distance between the respective bubble centers (as counted by the mean position of all associated vacancies) is less than 0.4 nm, or about 125% of the mean second-neighbor W–W distance.

3. Results and Discussion

We showed in previous publications [53, 54, 63] that surface orientation plays an important role in the depth distribution associated with helium plasma exposure—that is, the mean depth at which helium "slows down" to thermal velocities is a function of surface orientation. This is primarily due to effects such as channeling, that is, rapid motion of helium along crystallographic directions (primarily ⟨1 1 1⟩) without significant probability of non-glancing collisions with tungsten atoms (i.e., scattering). As such, {1 1 1} surfaces have the deepest depth distribution.

The effect of surface orientation is not limited to the initial depth distribution, but it is worth exploring what the preferred crystal orientation should be in a polycrystalline sample. Based solely on arguments of surface tension, one might deduce that {0 1 1} surfaces would dominate the crystal faces observed in real tungsten materials, as {0 1 1} surfaces have lower surface tension than all other crystal surfaces. This property is reproduced with the potential we employ in this study. On the other hand, {0 0 1} and {1 1 1} surfaces have higher surface tension than other surfaces, according to the calculations of Wang and coworkers [70]. With the particular inter-atomic potential we are using [56, 58, 59], the ordering of crystal surfaces according to their surface tensions is slightly different from the order from the calculations of Wang et al., though given the range of experimental values, the predictions are likely well within experimental uncertainty. These surface tension values are summarized in Table 2. When the initial conditions for these simulations were being selected, the low-index surfaces (0 0 1), (0 1 1), (1 1 1), and (2 1 1) were chosen in part because they spanned the breadth of surface tensions for available data in the literature, and in part because they spanned the range of depth distributions.

[Table 2 about here.]

3.1. Surface and Bubble Evolution

As discussed in our previous work [27], prismatic dislocation loop-punching is a major driving force of surface evolution in tungsten exposed to helium plasma. Generally, but not always, these loops have Burgers vectors $\vec{b} \in \frac{a}{2}\langle 1\,1\,1\rangle$, which means that for {0 0 1} surfaces, for which the four ⟨1 1 1⟩ directions pointing toward the plasma form $\approx 55°$ angles to the surface plane, the features due to a particular bubble will form a criss-cross pattern on the surface (see, for example, Sefta et al. [27], Figure 4). As discussed by Sandoval and coworkers [74], the rate

of such loop-punching is strongly dependent on the rate at which helium arrives at the bubble. As such, one might expect to see much more rapid surface deformation for bubbles near the surface than for similarly-sized bubbles farther below. This is indeed the case. However, what is perhaps unexpected is the fact that a surface feature can grow not just from one bubble or even a group of coincidentally placed bubbles whose ⟨1 1 1⟩ directions happen to intersect the surface at the same point. Instead, bubbles quite often form near—but not close enough to actually merge with—other bubbles, and in many cases, a mixed-Burgers-vector dislocation accompanies such a cluster of bubbles. The resulting prismatic loops, however, seem to find the surface as if the cluster of bubbles were a single bubble. This type of feature is clearly visible in Figure 2, which contains a cluster of 11 bubbles, no more than two of which appear to have formed by merging smaller bubbles together and all of which appear to have contributed to the same surface feature. This group of bubbles is highlighted in yellow in the center panes of Figure 2.

[Figure 2 about here.]

Another thing evident from Figure 2 is the fact that adatoms (which are whiter than the surface layer in the figure) do not always form in groups. In fact, isolated adatoms on this surface can form due to sub-surface bubbles, though it takes more than one helium atom in a cluster to nucleate a bubble and produce an adatom [34, 53]. By the time 1 μs elapses, we can see clear evidence of shelf-like features on the surface, which are indicative of loop-punching processes. However, these features are somewhat ill-defined and certainly nowhere near as pronounced as the flat sheets seen during forced bubble growth events with larger, over-pressurized bubbles in smaller simulations [27, 28]. The "island" features on the surface are typically traceable back to bubbles by following ⟨1 1 1⟩ directions back from the center of the feature (lines at 45° to the edge of the page in Figure 2 as drawn). This is easiest to see with the cluster highlighted in red (upper right corner) in Figure 2, which is responsible for the surface feature above and to its left on the page. The bubble of similar size closer to the corner of the box (shown in green) can be associated with a surface feature that spans the four corners of the box, spanning both sets of periodic boundary conditions.

The helium clusters highlighted in yellow in Figure 2 are all at approximately the same depth and horizontal position, yet as can clearly be seen in the center panes of figure, they do not merge into a single bubble despite being less than a bubble diameter apart in some cases.

However, they are, collectively, at least partially responsible for the large, barely-raised adatom island below and to their left on the page. The cluster itself is nearly planar—i.e., a disc of helium bubbles—rather than a spherical or cylindrical collection.

The three color-coded helium clusters in Figure 2 demonstrate three different growth patterns. The green bubble actually begins as three different bubbles—nucleated at 30, 60, and 100 ns, respectively—which slowly enlarge until they merge into a single bubble. The red cluster begins as two bubbles, which merge together some time between 260 ns and 270 ns to form a single bubble. The yellow cluster, as discussed, starts as individual bubbles and remains as such.

Perhaps the biggest surprise comes in the depth distributions. Unsurprisingly, we see large numbers of growing bubbles near the surface, at or slightly below the depth at which helium enters the simulation box. However, there is little or no growth of bubbles deeper than 10–12 nm beneath the original surface. For example, there are several bubbles that form at approximately 23 nm deep, but grow barely at all throughout the rest of the simulation. We will discuss this phenomenon further in Section 4.1.

[Figure 3 about here.]

Since the surface tension is so different for each of the surface orientations, let's consider a simulation with a (0 1 1) surface, shown in Figure 3. This surface has its $\langle 1\,1\,1\rangle$ directions at 35.3° from normal, with the two out-of-surface directions (i.e., the [1 1 1] and $[\overline{1}\,1\,1]$ directions) parallel to the edges of the page. We immediately observe that this surface has adatoms that generally occur in "islands" on the surface rather than as individual adatoms—this happens because of the significantly higher mobility of adatoms on {0 1 1} surfaces than for {0 0 1} surfaces, which in turn is because of the denser packing of atoms in {0 1 1} surfaces. This increased mobility means that lone adatoms, produced by small clusters of helium beneath the surface [53], diffuse relatively rapidly until they encounter another adatom. Di-adatom clusters still move, though less rapidly than single adatoms; mobility decreases as each atom is added. As such, some surface features—primarily those formed early-on in the simulation—are difficult to link to any particular bubble, as they are actually agglomerates of defects produced by several bubbles. Incidentally, the hop directions for surface diffusion of such highly-mobile adatoms are *also* $\langle 1\,1\,1\rangle$ crystallographic directions, which in this case are parallel to the plane of the surface (the $\pm[\overline{1}\,\overline{1}\,1]$ and $\pm[1\,\overline{1}\,1]$ directions).

Later in the simulation, once some of the near-surface bubbles have become large enough to start loop-punching (resulting in flat islands of adatoms growing up in ⟨1 1 1⟩ directions from the bubble), the "islands" these loop-punching processes create form sinks for individual, mobile adatoms, resulting in large, well-defined islands. As the bubbles grow larger and larger, the island may form second, third, and even higher layers. At approximately 1 μs, the highest feature is approximately five atomic layers high, or about 0.7 nm above the original surface. The resulting defect has a distinct "striped" pattern to it—that is, the islands are elongated in the vertical directions (as drawn), corresponding to elongation of features in ⟨1 1 1⟩ crystallographic directions.

As noted in the color-coded helium atoms in the second group of images in Figure 3, we observe once again that bubbles can start from single nucleation sites (green bubble), dual nucleation sites (yellow bubbles), or several nucleation sites that may not even result in a definable single bubble (red bubbles).

Similar to the trends in Figure 2, we see in the right-hand images in Figure 3 that there is almost immediately a population of small bubbles deep in the box (approximately 22 nm) that do not grow significantly. We also see similar growth of bubbles near the surface, though the largest bubble is much smaller.

[Figure 4 about here.]

The (1 1 1) surface is drastically different in character and appearance, before *and* after helium implantation, than the (0 1 1) surface. The results are shown in Figure 4. Bare, unimplanted, perfect {1 1 1} surfaces still look "flat" on the scale shown in Figure 4, though on closer inspection we clearly see three distinct layers of atoms. The ease of atomic rearrangement—one of the slip directions is perpendicular to the surface—means that this particular crystal face rearranges itself into tiny pyramid-like structures within a nanosecond or so of the onset of helium implantation. As helium is added to the system, this rearrangement becomes more pronounced: by 250 ns (upper left of Figure 4), we already see raised areas, which come from loop-punching associated with small bubbles near the surface; and recessed areas, which come from simple atomic rearrangements. These rearrangements can push the surface upward or downward, and can occur with or without the presence of helium atoms nearby. In fact, one small "divot" in the surface is as much as 1.2 nm *below* where the surface started by time 1 μs has elapsed.

It is significantly clearer that individual features are associated with bubbles for this surface, as the slip directions are normal to the surface (and therefore dislocation loops and interstitials are emitted straight toward the plasma from a bubble). For example, the group of bubbles highlighted in green in the second pane is directly responsible for the diffuse island directly above it. The yellow bubble, conversely, grows as a single bubble and results in a very localized tendril growing into the plasma, in this case approximately 1.3 nm high with a width of only 1.6 nm. This feature, like several others observed, gives the impression of the surface *trying* to make {1 1 0} facets—thereby minimizing surface free energy—while still relieving stress. The smaller features therefore resemble small pyramids, which eventually grow into dome-like structures if the bubble expands fast enough. The red bubble, which nucleates approximately 2.4 nm below the original surface, eventually bursts and releases its helium back to the plasma when the surface ligament thins to approximately 0.55 nm, which happens between 0.82 μs and 0.83 μs into the simulation. The surface feature from this bubble remains unchanged, however, and the path back to the surface almost immediately fills back in, allowing a small amount of helium to re-infiltrate to form a new bubble by the 1 μs mark. The bubble fills in almost to its original helium density after approximately 1.4 μs of total simulation time, though the bubble is slightly smaller than the one that burst initially (data not shown).

On the right-hand side of Figure 4, we see that there are fewer clusters below 15 nm or so than in Figures 2 and 3. This is due partially to the fact that the box is only about 21 nm deep in this simulation (shallower than all the others), and partially because it started even more shallow than that—our initial tungsten slab was only 15.98 nm thick, which we increased to 21.48 nm after 150 ns. In the rest of the depth distributions, however, we see similar evolution of bubbles between 5 nm deep and the bottom of the box as in the previously-discussed orientations. What is different about this depth distribution is the much larger numbers of bubbles near the surface, in particular at low fluences. This is due to what we have defined as "modified trap mutation," or growth of near-surface bubbles facilitated by the forces resulting from image stresses across the surface plane. This leads to increased helium segregation at the surface, as established in our previous publications [34, 53, 54, 75].

[Figure 5 about here.]

The results of plasma exposure simulations on tungsten with a (2 1 1) surface orientation are shown in Figure 5. It is evident after 250 ns that there are linear arrangements of adatoms that

form on this surface. This happens when individual interstitials are emitted to form adatoms due to the presence of near-surface bubbles—this has significant probability of occurrence for a single helium atom that is two layers below the surface, and occurs instantaneously when a di-helium cluster comes within four layers (about 0.37 nm), as discussed in a prior publication [53]—and those adatoms diffuse along the surface. Due to the corrugation of the (2 1 1) surface, the adatoms move relatively quickly in the $\pm[1\,1\,\bar{1}]$ directions (left/right) but very slowly in the $\pm[0\,\bar{1}\,1]$ directions (up/down). With this orientation, as in the (0 1 1) case, there is a significant drop in mobility for every adatom added to a group, thereby producing long, straight features early on in the simulation.

This surface also shows clear association between bubbles and surface features, though not quite as obviously so as for the (1 1 1) crystal face. This is because the ⟨1 1 1⟩ directions make $\approx 19.5°$ angles with the surface plane, meaning dislocation loops do not distort their shape as much when they encounter the surface as they do for {0 0 1} and {0 1 1} surfaces. While there is a slight tendency for surface features to "lean" to the left and right (i.e., ⟨1 1 1⟩ directions), it is nowhere near as pronounced as it is for (0 1 1) and (0 0 1) surfaces. This surface, like the (1 1 1) surface, shows large populations of small clusters very near the surface, corresponding to similar modified trap mutation processes (only this time at 19.5° to the surface normal rather than 0° to it as is the case for the (1 1 1) surface).

The (2 1 1) surface orientation shows several interesting bubble-growth phenomena, as highlighted by the color-coded bubbles in the center images of Figure 5. First, the red bubbles: there are very clearly two bubbles present initially, though they finally do merge together to form a single bubble some time around 0.87 μs. A third bubble also forms, this one at around 0.41 μs, and eventually merges with the larger ones as well. The surface feature formed by the casting off of prismatic loops from the two relatively large bubbles does indeed look like it came from two bubbles—there is a "lean" to the island's shape toward the lower-left corner of the image. However, by the time the bubbles have gotten close to merging (0.75 μs), that feature looks as though it came from a single bubble all along.

In contrast, the green-coded bubbles do not fully merge into a larger bubble, and produce a diffuse surface feature in line with the angles up from the bubbles. The yellow-coded bubbles, on the other hand, merge from a group of four distinct bubbles into one large bubble, producing a feature nearly 1.3 nm high above it on the surface (at approximately a 20° angle from the center of the bubble).

It is important to note that the corrections we made to the depth distributions [63] were not made prior to the commencement of the simulation with a (2 1 1) free surface, so all calculations herein showing (2 1 1) surfaces represent those with the erroneous depth distribution (which is uniformly about 60% deeper), as reported in our original paper [53].

3.2. Helium Retention

For each of the four surface orientations discussed in the previous section, we observed different patterns of surface deformation, as well as different helium bubble distributions near the surface. As we have noted in prior publications [53, 76], the amount of helium retained—that is, the number of helium atoms remaining in the tungsten simulation supercell divided by the total number of insertions at a particular point in time—varies drastically as a function of surface orientation. This is shown in Figure 6.

[Figure 6 about here.]

The dashed lines in Figure 6 are drawn based on a simulation using Xolotl [77], a continuum-based simulator of helium cluster dynamics in plasma-facing materials parameterized by a series of molecular statics and molecular dynamics calculations, as described in several recent publications [34, 35, 41, 54, 75, 78, 79]. In fact, the data presented herein are a primary source of benchmarks against which to check Xolotl's parameterization and implementation. In this particular set of simulations, we disallowed the formation of clusters larger than seven helium atoms, which means that *all* helium clusters are mobile. Drift terms, which increase the cluster transport rates toward the surface, were still active, but modified bubble nucleation and trap mutation were disallowed. This gives a base line of what the retention *would* be, without the effects of surface orientation on bubble nucleation rates near the surface, and provides an estimate of the differences in retention due solely to the initial depth distribution.

Since the depth distributions used in the simulations for the (2 1 1) surface corresponded to the values from Table 1 of Ref. 53, rather than the corrected values in Ref. 63, we also provide a Xolotl simulation of the associated depth distribution. The result with the original distribution from Ref. 53 are labeled (2 1 1)′ in Figure 6. This should also give a rough idea of the amount of retention that is attributable to the depth distribution alone, and the relative effect of the error that results from inaccuracies in the depth distribution.

It should be noted that the insertion rate is identical in each case, meaning the flux of helium atoms that do not scatter off (the "nominal flux," or the "embedded flux") on each of

the surfaces is nearly identical—the only differences are due to the fact that the surface area is not precisely 2500 nm^2 (50 nm × 50 nm), and instead varies between 2489 nm^2 for the (1 1 1) case and 2526 nm^2 for the (1 1 0) case. As such, there is little or no difference based solely on flux between the four orientations.

One small but important effect—which is demonstrated by the dashed lines in Figure 6—is the effect of mean depth on retention. It stands to reason, of course, that a surface with a deeper depth profile would have slightly increased retention, and that is indeed what is observed. However, this fact alone is not nearly enough to explain the *huge* discrepancy between the (1 1 1) and (2 1 1) cases versus the (0 0 1) and (0 1 1) cases. In particular, the 60–70% retention for (1 1 1) and (2 1 1) at low fluence against 20–25% for (0 0 1) and (0 1 1) are almost entirely because of the modified trap mutation and bubble nucleation phenomenon we discuss in previous work [41, 53].

Retention levels off and then begins to increase for (0 0 1) and (0 1 1) surfaces at $\Phi_{\text{nominal}} \sim 10^{18}$ m^{-2}. This fluence—which is likely a strong function of implantation flux and the pre-existing tungsten microstructure—corresponds to the formation of the first immobilized bubbles, which increase retention through self-trapping. The same phenomenon happens for the other two surface orientations as well, though it is washed out by the effect of the modified bubble nucleation and trap mutation processes near {2 1 1} and {1 1 1} surfaces.

As fluence increases, the retention from all four simulations appears to saturate. This is not surprising, as near-surface phenomena are less important than the growth of bubbles as fluence increases.

3.3. Evolution of the Helium Depth Distribution

[Figure 7 about here.]

The progressive evolution of the helium depth distribution as a function of time is shown in Figure 7. While the (0 0 1) surface *begins* as the "deepest" depth distribution at low fluence (i.e., short times), it rapidly "catches up" and eventually is statistically similar if not identical to the other distributions. This underscores the observation that near-surface phenomena are not nearly as important at high fluence—only the pattern of surface features formed by sub-surface bubbles is significantly different between surface orientations.

Conversely, the (1 1 1) and (2 1 1) surfaces show a shallow distribution of helium that does not evolve significantly. Bubbles grow deeper, as with all four simulations, but the "knee" that is prominent early in the simulation is still present at 1 μs as well.

3.4. Bubble Growth Trajectories

Similar to the bubble size distributions in Figures 2–5, we attempted to track the size of each bubble as a function of time (see Section 2.3 for a description of how this is done). The end result is a trajectory for individual bubbles, giving us a very good indicator of how much pressure (that is, density) can build up inside the bubble before it trap mutates or loop-punches to create a larger bubble. This is extremely important information to have for continuum and coarse-grained models for two reasons. First, it provides an estimate of the rates of bubble growth over time, providing a benchmark against which to check results. Second, it provides a hard limit on the parameter space that needs to be considered. For example, a reaction–diffusion scheme with 100,000 species at every grid point is likely impossible to store in memory, but if we can eliminate all but a handful of those species as not ever existing, the calculation becomes much more tractable.

[Figure 8 about here.]

The number of bubbles present in these simulations yields too many trajectories (and overlapping colors) to plot all at once, so we have instead picked out the trajectories of the red and green bubbles in Figure 2, which are the two largest bubbles in that simulation, and plotted them in Figure 8.

It is apparent that all the bubbles in this example are within a narrow band of V/He ratios once they grow beyond about 30 vacancies or so. As the bubble grows, the threshold pressure for loop-punching seems to go down, which makes sense in the context of surface energy [28]. That being said, the bubble color-coded red in Figure 2 shows very few loop-punching events that can be specifically associated with the five (non-simultaneously existing) bubbles that eventually merge to form one. Instead, the surface features nearby seem to come from a group of nearby bubbles as well. However, the overall V/He ratio stays relatively similar throughout the process for both bubbles, holding steady in the 0.3–0.5 range. Perhaps most important, this ratio decreases as the bubble grows larger, though this could very well be due to the proximity of these particular bubbles to the surface. In fact, the center off mass of the bubble color-coded in green starts at 2.5–2.7 nm from the surface, moves up to 2.2 nm below once the two bubbles merge and the first loop-punching event occurs, and is finally only 1.7 nm below the original surface after 1 μs has elapsed. This is to be expected, given the nature of loop-punching and surface annihilation, but it might pose a means to track bubbles and/or test this mechanism experimentally. It should be noted that the region directly above both bubbles does not increase

significantly in height because of the fact that prismatic loops emitted by the bubbles end up in the region around the bubble, rather than right above it.

This sort of analysis could be done for other bubbles as well. In fact, from the perspective of benchmarks for coarse-grained models, it is important to know the range of sizes and V/He ratios for *all* bubbles observed in the system, not just the large ones. Since we anticipate very different distributions near the surface than far away from it, we have plotted bubbles within 4 nm of the surface in Figure 9 and bubbles deeper than 4 nm in Figure 10.

[Figure 9 about here.]

The near-surface bubbles (Figure 9) are generally within a "stripe" drawn around He/V= 3, though this line starts to "lean" to the right as the bubbles get bigger. For reference, the two uppermost groups of points in Figure 9*a* are the same bubbles whose growth is charted in Figure 8 (the green- and red-colored bubbles in Figure 2). Note that a point is drawn in this figure for each bubble at each time sampled, with times sampled every 1000 insertions (10 ns) between 0 and 1 μs. The swatches of bubbles in the off-diagonal areas, particularly those with very high V/He ratios, are indicative of bubbles that have burst and then partially filled back in. This happens on all surfaces, though it happens to be very obvious for at least two or three bubbles in the simulation with (0 0 1) orientation.

The tendency of {1 1 1} surfaces to permit facile movement of dislocation loops and tungsten interstitials straight upward, thereby allowing bubbles to grow incrementally (and linearly) straight upward, is apparent by the vertical nature of the bubble growth trajectories—for this surface, bubbles tend to fill, bit by bit, with helium until the loop-punching threshold is reached, at which point the bubble expands and the process starts over again. Because a ⟨1 1 1⟩ crystallographic direction is straight up, the threshold for loop-punching is likely less depth-dependent and/or lower in energy, though we do not estimate it quantitatively here.

[Figure 10 about here.]

In the bubbles farther beneath the surface, we see less of a tendency for those under the (1 1 1) surface to grow in small increments in helium followed by larger changes in vacancy number (as is seen frequently for those closer to the surface), though one bubble—the largest one in this plot—is doing so here. This indicates that for at least one bubble, the surface is close enough that bubble growth is made easier in the direction of the surface. However, we see the

same tight clustering of He/V ratios, with most larger bubbles lying between He/V = 2 and He/V = 3, and with smaller bubbles lying between He/V = 1 and He/V = 9.

The relatively narrow band of V/He ratios seen in Figures 9 and 10 is an important physical phenomenon for coarse-grained modeling, as it indicates that a large section of the parameter space does not need to be included: anything with He/V $>$ 4 will clearly never form once bubbles get bigger than approximately 50 vacancies, and anything with He/V $>$ 3.5 or so is unlikely to be observed once bubbles exceed 75 vacancies or so. On the other end, bubbles with He/V $<$ 2 are effectively absent for nearly all surfaces (in the absence of bubble-bursting).

Unfortunately, even this reduced parameter space would still require extreme resources to store and process the resulting continuum-based simulation, in which all unique "species"—that is, He_x–V_y combinations for $x/y \in (2, 9)$ with the restrictions $x/y \in (2, 4)$ for $y > 50$ and $x/y \in (2, 3.5)$ for $y > 75$. With this in mind, we present a *mean* bubble growth trajectory for far-from-surface bubbles in Figure 11.

[Figure 11 about here.]

We only show the average density for bubbles smaller than 80 vacancies, as larger bubbles typically have only one bubble of that size present throughout all four simulations and thus reporting an average makes less sense. Because of the statistics associated with these numerous, smaller bubbles, the average is very precise, so the error bars are often smaller than the markers themselves—this just means the *average* is very well-known, of course, not necessarily that the distribution of bubble densities is particularly narrow. To guide the eye and provide a means of estimation of mean bubble density as a function of vacancy number, we estimate that

$$n_{\mathrm{He}} = 5 n_{\mathrm{V}}^{0.86}, \tag{3}$$

where n_{He} is the number of helium atoms in a given bubble and n_{V} is the number of vacancies associated with the same bubble, is a reasonable fit to the mean bubble density on the interval 0–80 vacancies, as shown in Figure 11. Equation (3) is actually a reasonable fit to individual bubbles of sizes up to $n_{\mathrm{V}} = 300$, the largest bubbles found greater than 4 nm below the surface in the first microsecond of these simulations.

One very obvious result of these bubble growth trajectories is that continuum models that track bubble sizes according to both number of helium atoms and number of vacancies need only track a relatively narrow band of He:V ratios. The "optimum" ratio appears to change

over time, starting near 7:1 but decreasing to 4:1, 3:1, and eventually closer to 2:1 as bubble size and surface area grow.

4. Additional Discussion

The results presented in the previous section have implications for both simulations and experimental studies of plasma-facing tungsten. We will discuss some of those implications in this section.

4.1. Growth of Deep Bubbles

While the pattern of surface deformation in Figures 2–5 might seem intriguing and/or convincing at first as an explanation for tungsten fuzz, it is worth mentioning that the tallest feature is only 1.3 nm high and only about 1.6 nm wide. These dimensions are *very* far from the ≈ 65 nm-wide fuzz tendrils observed experimentally [18], which naturally poses the question as to how exactly 1.6 nm-wide tendrils on a 50 nm (periodic) slab would translate into 65 nm-wide tendrils in reality. Indeed, since the first experimental snapshot is taken at $\sim 10^8$ times longer in time than the present simulations, we will never get a direct answer using these methods.

However, the "flat" cluster size profile seen early-on in the upper-right-hand images of Figures 2–5 raises several questions. At this flux—and bear in mind that these simulations are only a factor of 20–30 higher in flux than that expected in ITER if we include reflections—we see very, very slow bubble growth at anything below 12 nm, despite the fact that the simulation box is almost 25 nm deep. This observation suggests something is missing—or more correctly, inactive at the point of one microsecond or at least at the corresponding fluences—from the simulations. If bubbles are responsible for tungsten fuzz—and we are under the strong belief at this point that they are—then how do $\sim$ 10–100 nm bubbles form far enough beneath surfaces that they can create such defects, particularly if the growth rate of bubbles more than 12 nm below the surface is extremely slow due to "shielding" by bubbles farther up?

We speculate that the answer to the deep diffusion question comes from two points. First, it is clear from the cluster size distributions at 0.25 μs and earlier that the first few nanoseconds—or perhaps the first few nanoseconds after a bubble bursting event, for example—are critical in establishing a population of helium atoms well below the insertion depth. On systems that are microns or even millimeters on a side, rather than tens of nanometers, the population of such bubbles would be significant. Second, we have long assumed that the density of helium

bubbles deep in the simulation cell would deepen over time, with no particular levels present early in the simulation. However, as should be evident from Figure 12, which shows the bubble size distributions at very short times—10 ns into the simulation—the rate of diffusion of small helium clusters greatly exceeds the rate of bubble formation, to the point that there is still a cluster or two of helium atoms nearly at the bottom of the simulation box a mere 10 ns in. As such, it may be appropriate to reconsider the assumption that there is insufficient helium present to nucleate bubbles deep within the material—even in these simulations, the absolute depth is much more limited by the finite size of the slab than it is by the rate of helium transport in simulations of this size and flux. We will explore the effects of lower flux in a future study.

[Figure 12 about here.]

One obvious step in response to the observation of bubbles "blocking" deep diffusion is to drop the flux down even further, even closer to experimental values. We will explore the direct effect of flux on cluster sizes in a future publication. However, dropping the flux won't solve the underlying problem of the 4–5 orders of magnitude in fluence between simulations and current experiments (and in fact will make it worse). While this study narrows the gap in real time by two orders of magnitude or so, the fluences seen here are perhaps a factor of ten higher than in other previously reported molecular dynamics studies and at least 10^4 m^{-2} *lower* than even the lowest-fluence experiments. Addressing this "fluence gap" should be a target of future work, both from the simulation and experimental communities.

One connection we *can* make is that the very earliest pictures of fuzz—times on the order of 400 s or so—show what appears to be tiny, $\approx$ 50 nm diameter bubbles and corresponding surface roughness nearby (see, for example, Kajita and cowokers [18], Figures 2*a* and 2*a′*). This is consistent with the simulation results, though we are talking about features seen experimentally that are approximately 10–50 times larger than anything observed at this fluence in the simulations.

The observation of deep-down bubbles creating dislocation loops that can later partially or completely "fill in" recently burst bubbles may help to explain the apparent self-similarity of experimental surfaces to those herein. However, any thorough conclusions about the growth of such bubbles, which are sizes approaching the size of the entire simulation box in this work, remain as conjecture requiring further study.

4.2. *Surface Feature Evolution*

The rudimentary surface features observed in Figures 2–5 strongly suggest that regions of the surface with {1 1 0} orientation will have relatively "smooth" features that "slant" in ⟨1 1 1⟩ directions. Similarly, {1 1 1} surfaces should have features that grow straight up, but that eventually yield to triangular faceting. This forms pyramidal structures with {1 1 0} facets. These pyramidal structures—or at least the tendency to deform the material to form {1 1 0} facets for the purposes of surface energy minimization—may eventually grow to resemble something like the pyramidal structures observed experimentally by Parish and coworkers [50]. In particular, the "pile up" of features on {2 1 1} surfaces (Figure 5)—-or similar facile adatom diffusion in one direction yet impeded at right angles to it—will likely result in the "wave" or "terrace" morphologies they observed.

Unfortunately, it is difficult if not impossible to justify or refute the observation, made by Parish and coworkers [50], that {0 0 1} surfaces form pyramid-like structures. It's conceivable that such features form later, after the bubble density becomes great enough that the dislocations themselves become trapped by other bubbles, but at the length and time scale of 50 nm and 1 μs, the {0 0 1} surface appears to have the *least* well-defined surface deformation pattern.

What we are certain of in this context is that surface orientation plays an important role in the shape, height, distribution, and morphology of surface features formed on tungsten surfaces in the initial stages of helium plasma exposure. This surface orientation effect has been observed experimentally [48, 50], though without the context as to the specific mechanisms involved. The orientation dependence is due to (a) differences in initial penetration depth due to channeling and similar phenomena, (b) relative rates of diffusion of adatoms, and (c) angle at which ⟨1 1 1⟩-oriented prismatic dislocation loops intersect the surface.

4.3. *Relation to "Incubation Fluence" of Tungsten Fuzz*

A recent article by Petty and coworkers [80] suggested a modification of the "conventional wisdom" they themselves had put forward years earlier: rather than the thickness of tungsten "fuzz" growing as $z \propto t^{1/2}$, it instead appears to lag well behind that value until a certain "incubation fluence," Φ_0, is reached, meaning $z \propto (\Phi - \Phi_0)^{1/2}$. This incubation fluence was reported to be $\Phi_0 \sim 10^{24}$ m^{-2} for fluxes $\Gamma \sim 10^{22}$ m^{-2} s^{-1}, corresponding to $t \sim 100$ s.

Based on the results presented in Section 3, we suggest that this "incubation" period is due to the fact that it takes a certain period of time for helium atoms to diffuse—in the form of small, mobile clusters of fewer than eight helium atoms—deep enough into the material to

where bubbles that are, say, 10–100 nm in diameter can form without immediately bursting through to the surface. The fact that near-surface bubbles, which at ITER-like fluxes will form a layer in approximately the same position as that shown in Figures 2–5, effectively block the growth of bubbles further down suggests that significantly longer times than 1 μs—and significantly deeper simulation supercells than the 25 nm–deep ones studied here—are required if one wishes to observe anything even approaching the scale of fuzz. It bears mentioning, of course, that the average "tendril" observed on tungsten surfaces after helium plasma exposure in linear plasma devices is approximately the same size as the entire simulation box for the simulations presented here.

We are unable to ascertain, based on our results, the presence or absence of "wavy" features on surfaces, as observed by Ohno and coworkers [48]; they observed no such features on {3 1 0}, {2 1 0}, {7 4 0}, and {3 2 0} surfaces, but found wavy features on {1 0 0}, {2 1 1}, {1 1 0}, and {1 1 1}. Since we (unwittingly) only simulated the surfaces they *did* find features on, it might be interesting to conduct a similar study on the other four orientations; depth distributions have already been published for all but {7 4 0} surfaces [53, 63]. We are, however, in complete agreement with their hypothesis that surface features are pushed up in different angles on different surfaces (cf. Figure 6 of Ref. 48).

One materials question that arises from this study is the importance of *groups* of bubbles, such as the group highlighted in yellow in Figure 2, on surface features. This is particularly important in lieu of the observation that helium is attracted to, and immobilizes, prismatic dislocation loops [81]. Such prismatic loops are produced every time a surface feature forms, and after the initial 100 ns or so, are produced very frequently—perhaps one every 10 ns or even faster in our 50 nm × 50 nm surface—so there is ample opportunity for loops to become trapped by helium below the surface, annihilate inside voids, or intersect with other mobile loops.

5. Summary and Conclusions

The surface response and near-surface structural response of W{0 0 1}, W{0 1 1}, W{1 1 1}, and W{2 1 1} surfaces to helium implantation is very different between surface orientations at times of order 1 μs. In particular, the shape of various features on the surface and their tendencies to "lean" or extend in a particular direction is very different, and the degree and mechanism of helium retention is drastically different among different surface orientations.

The difference in mechanism between the surfaces was reported previously [53, 63], but the ramifications of these differences in mechanism leads to pyramidal structures on {1 1 1} surfaces (as bubble-induced features attempt to form low-surface-tension {0 1 1} surface features); sheet-like features on {0 0 1} and {0 1 1} surfaces; and simply higher-up surfaces on {2 1 1} surfaces. Features from the bursting of bubbles are not yet obvious at 1 μs, and their cumulative effects are weak at this flux/fluence combination.

The shape and delineation of each surface is more obviously a dislocation loop (i.e., a flat, roughly circular plane of "extra" atoms) in the case of {0 1 1} and {0 0 1} surfaces. In {1 1 1} surfaces, the islands formed by the same mechanism are more pyramidal and/or hemispherical, in agreement with previous studies of much larger, more highly over-pressurized bubbles [28]. In {2 1 1} surfaces, the shape of the "island" is harder to make out, and the features have "appendages" that appear to reach out along crystallographic vectors. This is in part due to the very corrugated appearance of the (2 1 1) surface, as any stress that can be relieved by forcing tungsten atoms between "ridges" will manifest as additional "ridge" features (that are merely one extra atom high) in the $\pm[1\,\bar{1}\,\bar{1}]$ directions.

The initial depth distributions are sharply different due to near-surface trap mutation (adatom/vacancy pair formation), but this effect becomes less and less important as fluence increases. We find, independent of surface orientation, that bubbles typically grow in a relatively narrow band of He/V ratios, with He/V starting in the 1–9 range and slowly narrowing to 2–3 as the bubble size increases. Bubbles greater than 120 vacancies are almost universally in the He/V $\in [2, 3]$ range.

Future work will discuss the pronounced influence of grain boundaries and flux on the phenomena observed in this work, as well as the interaction of sub-surface helium bubbles with additional helium and/or hydrogen.

Acknowledgments

This material is based upon work supported by the U. S. Department of Energy, Office of Science, Office of Fusion Energy Sciences, and Office of Advanced Scientific Computing Research through the Scientific Discovery through Advanced Computing (SciDAC) project on Plasma–Surface Interactions through Oak Ridge National Laboratory and award number DE-SC0008875, as well as subcontract 4000135920 through Oak Ridge National Laboratory.

This work used massive amounts of computing resources at the National Energy Research Scientific Computing Center (NERSC), a DOE Office of Science User Facility supported by the Office of Science of the U. S. Department of Energy under Contract No. DE-AC02-05CH11231.

ORNL is managed by UT–Battelle, LLC for the U. S. Department of Energy under Contract No. DE-AC05-00OR22725.

[1] ITER: The way to new energy, http://www.iter.org/ (2012).

[2] F. W. Perkins, D. E. Post, N. A. Uckan, M. Azumi, D. J. Campbell, N. Ivanov, N. R. Sauthoff, M. Wakatani, W. M. Nevins, M. Shimada, J. Van Dam, D. Boucher, G. Cordey, A. Costley, J. Jacquinot, G. Janeschitz, S. Mirnov, V. Mukhovatov, G. Porter, D. Post, S. Putvinski, M. Shimada, R. Stambaugh, M. Wakatani, J. Wesley, K. Young, R. Aymar, Y. Shimonmura, D. Boucher, A. Costley, N. Fujisawa, Y. Igitkhanov, G. Janeschitz, A. Kukushkin, V. Mukhovatov, F. Perkins, D. Post, S. Putvinski, M. Rosenbluth, J. Wesley, ITER physics basis. chapter 1: Overview and summary, Nucl. Fusion 39 (12) (1999) 2137–2174. doi:10.1088/0029-5515/39/12/301.

[3] G. Federici, C. H. Skinner, J. N. Brooks, J. P. Coad, C. Grisolia, A. A. Haasz, A. Hassanein, V. Philipps, C. S. Pitcher, J. Roth, W. R. Wampler, D. G. Whyte, Plasma–material interactions in current tokamaks and their implications for next step fusion reactors, Nucl. Fusion 41 (12) (2001) 1967–2136. doi:10.1088/0029-5515/41/12/218.

[4] H. Bolt, V. Barabash, W. Krauss, J. Linke, R. Neu, S. Suzuki, N. Yoshida, ASDEX Upgrade Team, Materials for the plasma-facing components of fusion reactors, J. Nucl. Mater. 329–333 (2004) 66–73. doi:10.1016/j.jnucmat.2004.04.005.

[5] G. Janeschitz, Plasma–wall interaction issues in ITER, J. Nucl. Mater. 290–293 (2001) 1–11. doi:10.1016/S0022-3115(00)00623-1.

[6] S. Suzuki, Y. Ueda, K. Tokunaga, K. Sato, M. Akiba, Present research status on divertor and plasma facing components for fusion power plants, Fusion Sci. Tech. 44 (1) (2003) 41–48.

[7] M. Kikuchi, K. Lackner, M. Q. Tran (Eds.), Fusion Physics, International Atomic Energy Agency, Vienna, 2012.

[8] J. F. Ziegler, J. P. Biersack, M. D. Ziegler, SRIM: The Stopping and Range of Ions in Matter, Lulu Press, Morrisville, NC, 2008, http://www.srim.org/.

[9] H. Iwakiri, K. Yasunaga, K. Morishita, N. Yoshida, Microstruture evolution in tungsten during low-energy helium ion radiation, J. Nucl. Mater. 283–287 (2000) 1134–1138. doi:10.1016/S0022-3115(00)00289-0.

[10] K. Tokunaga, R. P. Doerner, R. Seraydarian, N. Noda, Y. Kubota, N. Yoshida, T. Sogabe, T. Kato, B. Schedler, Surface morphology and helium retention on tungsten exposed to low energy and high flux helium plasma, J. Nucl. Mater. 313–316 (2003) 92–96. doi:10.1016/S0022-3115(02)01362-4.

[11] M. Miyamoto, D. Nishijima, Y. Ueda, R. P. Doerner, H. Kurishita, M. J. Baldwin, S. Morito, K. Ono, J. Hanna, Observations of suppressed retention and blistering for tungsten exposed to deuterium–helium mixture plasmas, Nucl. Fusion 49 (6) (2009) 065035. doi:10.1088/0029-5515/49/6/065035.

[12] D. Nishijima, M. Y. Ye, N. Ohno, S. Takamura, Formation mechanism of bubbles and holes on tungsten surface with low-energy and high-flux helium plasma irradiation in NAGDIS-II, J. Nucl. Mater. 329–333 (Part B) (2004) 1029–1033. doi:10.1016/j.jnucmat.2004.04.129.

[13] W. Sakaguchi, S. Kajita, N. Ohno, M. Takagi, In situ reflectivity of tungsten mirrors under helium plasma exposure, J. Nucl. Mater. 390–391 (2009) 1149–1152. doi:10.1016/j.jnucmat.2009.01.276.

[14] S. Kajita, S. Takamura, N. Ohno, D. Nishijima, H. Iwakiri, N. Yoshida, Sub-ms laser pulse irradiation on tungsten target damaged by exposure to helium plasma, Nucl. Fusion 47 (9) (2007) 1358–1366. doi:10.1088/0029-5515/47/9/038.

[15] S. Takamura, N. Ohno, D. Nishijima, S. Kajita, Formation of nanostructured tungsten with arborescent shape due to helium plasma irradiation, Plasma Fusion Res. 1 (2006) 051. doi:10.1585/pfr.1.051.

[16] M. J. Baldwin, R. P. Doerner, Helium induced nanoscopic morphology on tungsten under fusion relevant plasma conditions, Nucl. Fusion 48 (3) (2008) 035001. doi:10.1088/0029-5515/48/3/035001.

[17] M. J. Baldwin, R. P. Doerner, D. Nishijima, K. Tokunaga, Y. Ueda, The effects of high fluence mixed-species (deuterium, helium, beryllium) plasma interactions with tungsten, J. Nucl. Mater. 390–391 (2009) 886–890. doi:10.1016/j.jnucmat.2009.01.247.

[18] S. Kajita, W. Sakaguchi, N. Ohno, N. Yoshida, T. Saeki, Formation process of tungsten nanostructure by the exposure to helium plasma under fusion relevant plasma conditions, Nucl. Fusion 49 (9) (2009) 095005. doi:10.1088/0029-5515/49/9/095005.

[19] G. M. Wright, D. Brunner, M. J. Baldwin, R. P. Doerner, B. Labombard, B. Lipschultz, J. L. Terry, D. G. Whyte, Tungsten nano-tendril growth in the Alcator C-Mod divertor, Nucl. Fusion 52 (4) (2012) 042003. doi:10.1088/0029-5515/52/4/042003.

[20] G. M. Wright, D. Brunner, M. J. Baldwin, K. Bystrov, R. P. Doerner, B. Labombard, B. Lipschultz, G. ~~DeTemmerman~~De Temmerman, J. L. Terry, D. G. Whyte, K. B. Woller, Comparison of tungsten nano-tendrils grown in Alcator C-Mod and linear plasma devices, J. Nucl. Mater. 438 (2013) S84–S89. doi:10.1016/j.jnucmat.2013.01.013.

[21] T. J. Petty, J. W. Bradley, Tungsten nanostructure formation in a magnetron sputtering device, J. Nucl. Mater. 453 (1–3) (2014) 320–322.

[22] M. J. Baldwin, R. P. Doerner, Formation of helium induced nanostructure 'fuzz' on various tungsten grades, J. Nucl. Mater. 404 (3) (2010) 165–173. doi:10.1016/j.jnucmat.2010.06.034.

[23] M. Yamagiwa, S. Kajita, N. Ohno, M. Takagi, N. Yoshida, R. Yoshihara, W. Sakaguchi, H. Kurishita, Helium bubble formation on tungsten in dependence of fabrication method, J. Nucl. Mater. 417 (2011) 499–503. doi:10.1016/j.jnucmat.2011.02.007.

[24] K. Tokunaga, M. J. Baldwin, R. P. Doerner, D. Nishijima, H. Kurishita, T. Fujiwara, K. Araki, Y. Miyamoto, N. Ohno, Y. Ueda, Nanoscale surface morphology of tungsten materials induced by Be-seeded D-He plasma exposure, J. Nucl. Mater. 417 (1–3) (2011) 528–532. doi:10.1016/j.jnucmat.2011.01.078.

[25] S. J. Zenobia, G. L. Kulcinski, Formation and retention of surface pores in helium-implanted nano-grain tungsten for fusion reactor first-wall materials and divertor plates, Phys. Scr. T138 (2009) 014049. doi:10.1088/0031-8949/2009/T138/014049.

[26] O. El-Atwani, M. Efe, B. Heim, J. P. Allain, Surface damage in ultrafine and multimodal grained tungsten materials induced by low energy helium irradiation, J. Nucl. Mater. 434 (1–3) (2013) 170–177. doi:10.1016/j.jnucmat.2012.11.012.

[27] F. Sefta, K. D. Hammond, N. Juslin, B. D. Wirth, Tungsten surface evolution by helium bubble nucleation, growth, and rupture, Nucl. Fusion 53 (7) (2013) 073015. ~~doi:10.1016/j.jnucmat.2013.01.101~~doi:10.1088/0029-5515/53/7/073015.

[28] F. Sefta, N. Juslin, B. D. Wirth, Helium bubble bursting in tungsten, J. Appl. Phys. 114 (24) (2013) 243518. doi:10.1063/1.4860315.

[29] A. M. Ito, Y. Yoshimoto, S. Saito, A. Takayama, H. Nakamura, Molecular dynamics simulation of a helium bubble bursting on tungsten surfaces, Phys. Scr. T159 (2014) 014062. doi:10.1088/0031-8949/2014/T159/014062.

[30] J. Cui, M. Li, J. Wang, Q. Hou, Molecular dynamics study of helium bubble pressure in tungsten, Nucl. Instrum. Meth. Phys. Res. B 352 (2015) 104–106. doi:10.1016/j.nimb.2014.12.025.

[31] B. L. Zhang, J. Wang, M. Li, Q. Hou, A molecular dynamics study of helium bubble formation and gas release near titanium surfaces, J. Nucl. Mater. 438 (1–3) (2013) 178–182. doi:10.1016/j.jnucmat.2013.03.033.

[32] F. Sefta, N. Juslin, K. D. Hammond, B. D. Wirth, Molecular dynamics simulations on the effect of sub-surface helium bubbles on the sputtering yield of tungsten, J. Nucl. Mater. 438 (2013) S493–S496. doi:10.1016/j.jnucmat.2013.01.101.

[33] F. Ferroni, K. D. Hammond, B. D. Wirth, Sputtering yields of pure and helium-implanted tungsten under fusion-relevant conditions calculated using molecular dynamics, J. Nucl. Mater. 458 (2015) 419–424. doi:10.1016/j.jnucmat.2014.12.090.

[34] L. Hu, K. D. Hammond, B. D. Wirth, D. Maroudas, Dynamics of small mobile helium clusters near tungsten surfaces, Surf. Sci. 626 (2014) L21–L25. doi:10.1016/j.susc.2014.03.020.

[35] L. Hu, K. D. Hammond, B. D. Wirth, D. Maroudas, Interactions of mobile helium clusters with surfaces and grain boundaries of plasma-exposed tungsten, J. Appl. Phys. 115 (2014) 173512. doi:10.1063/1.4874675.

[36] K. D. Hammond, L. Hu, D. Maroudas, B. D. Wirth, Helium impurity transport on grain boundaries: Enhanced or inhibited?, Europhys. Lett. 110 (2015) 52002. doi:10.1209/0295-5075/110/52002.

[37] X.-C. Li, X. Shu, P. Tao, Y. Yu, G.-J. Niu, Y. Xu, F. Gao, G.-N. Luo, Molecular dynamics simulation of helium cluster diffusion and bubble formation in bulk tungsten, J. Nucl. Mater. 455 (2014) 544–548. doi:10.1016/j.jnucmat.2014.08.028.

[38] Y. L. Zhou, J. Wang, Q. Hou, A. H. Deng, Molecular dynamics simulations of the diffusion and coalescence of helium in tungsten, J. Nucl. Mater. 446 (1–3) (2014) 49–55. doi:10.1016/j.jnucmat.2013.11.034.

[39] L. Sandoval, D. Perez, B. P. Uberuaga, A. F. Voter, Competing kinetics and He bubble morphology in W, Phys. Rev. Lett. 114 (2015) 105502. doi:10.1103/PhysRevLett.114.105502.

[40] R. Kobayashi, T. Hattori, T. Tamura, S. Ogata, A molecular dynamics study on bubble growth in tungsten under helium irradiation, J. Nucl. Mater. 463 (2015) 1071–1074. doi:10.1016/j.jnucmat.2014.12.049.

[41] L. Hu, K. D. Hammond, B. D. Wirth, D. Maroudas, Molecular-dynamics analysis of mobile helium cluster reactions near surfaces of plasma-exposed tungsten, J. Appl. Phys. 118 (16) (2015) 163301. doi:10.1063/1.4933393.

[42] K. O. E. Henriksson, K. Nordlund, J. Keinonen, D. Sundholm, M. Patzschke, Simulations of the initial stages of blistering in helium implanted tungsten, Phys. Scr. T108 (2004) 95–98. doi:10.1238/Physica.Topical.108a00095.

[43] K. O. E. Henriksson, K. Nordlund, J. Keinonen, Molecular dynamics simulations of helium cluster formation on tungsten, Nucl. Instrum. Meth. Phys. Res. B 244 (2) (2006) 377–391. doi:10.1016/j.nimb.2005.10.020.

[44] F. Sefta, Surface response of tungsten to helium and hydrogen plasma flux as a function of temperature and incident kinetic energy, Ph.D. dissertation, University of California, Berkeley, Berkeley (2014).

[45] A. Lasa, K. O. E. Henriksson, K. Nordlund, MD simulations of onset of tungsten fuzz formation under helium irradiation, Nucl. Instrum. Meth. Phys. Res. B 303 (2013) 156–161. doi:10.1016/j.nimb.2012.11.029.

[46] L. Pentecoste, P. Brault, A.-L. Thomann, P. Desgardin, T. Lecas, T. Belhabib, M.-F. Barthe, T. Sauvage, Low energy and low fluence helium implantations in tungsten: Molecular dynamics simulations and experiements, J. Nucl. Mater. 470 (2016) 44–54. doi:10.1016/j.jnucmat.2015.12.017.

[47] D. Nishijima, M. J. Baldwin, R. P. Doerner, J. H. Yu, Sputtering properties of tungsten 'fuzzy' surfaces, J. Nucl. Mater. 415 (2011) S96–S99. http://dx.doi.org/10.1016/j.jnucmat.2010.12.017 doi:10.1016/j.jnucmat.2010.12.017.

[48] N. Ohno, Y. Hirahata, M. Yamagiwa, S. Kajita, M. Takagi, N. Yoshida, R. Yoshihara, T. Tokunaga, M. Tokitani, Influence of crystal orientation on damages of tungsten exposed to helium plasma, J. Nucl. Mater. 438 (2013) S879–S882. doi:10.1016/j.jnucmat.2013.01.190.

[49] S. Narita, N. Ezumi, N. Ohno, Y. Uesugi, S. Takamura, High heat flux plasma generator for new divertor plasma simulator in Nagoya University, in: Proceedings of the 1996 International Conference on Plasma Physics, Nagoya, Japan, 1996, pp. 1362–1365.

[50] C. M. Parish, H. Hijazi, H. M. Meyer, F. W. Feyer, Effect of tungsten crystallographic orientation on He-ion-induced surface morphology changes, Acta Mater. 62 (1) (2014) 173–181. doi:10.1016/j.actamat.2013.09.045.

[51] D. Donovan, D. Buchenauer, J. Whaley, R. Friddle, Characterization of a compact ECR plasma source and its applications to studies of helium ion damage to tungsten, Phys. Scr. T167 (2016) 014040. doi:10.1088/0031-8949/T167/1/014040.

[52] A. M. Ito, A. Takayama, Y. Oda, T. Tamura, R. Kobayashi, T. Hattori, S. Ogata, N. Ohno, S. Kajita, M. Yajima, Y. Noiri, Y. Yoshimoto, S. Saito, S. Takamura, T. Murashima, M. Miyamoto, H. Nakamura, Hybrid simulation research on formation mechanism of tungsten nanostructure induced by helium plasma irradiation, J. Nucl. Mater. 463 (2015) 109–115. doi:10.1016/j.jnucmat.2015.01.018.

[53] K. D. Hammond, B. D. Wirth, Crystal orientation effects on helium ion depth distributions and adatom formation processes in plasma-facing tungsten, J. Appl. Phys. 116 (14) (2014) 143301. doi:10.1063/1.4897419.

[54] D. Maroudas, S. Blondel, L. Hu, K. D. Hammond, B. D. Wirth, Helium segregation on surfaces of plasma-exposed tungsten, J. Phys. Condens. Matter 28 (6) (2016) 064004. doi:10.1088/0953-8984/28/6/064004.

[55] S. Plimpton, Fast parallel algorithms for short-range molecular dynamics, J. Comput. Phys. 117 (1) (1995) 1–19, http://lammps.sandia.gov/. doi:10.1006/jcph.1995.1039.

[56] M. W. Finnis, J. E. Sinclair, A simple empirical *N*-body potential for transition metals, Philos. Mag. A 50 (1) (1984) 45–55. doi:10.1080/01418618408244210.

[57] M. W. Finnis, J. E. Sinclair, Erratum: A simple empirical *N*-body potential for transition metals, Philos. Mag. A 53 (1) (1986) 161. doi:10.1080/01418618608242815.

[58] G. J. Ackland, R. Thetford, An improved *N*-body semi-empirical model for body-centred cubic transition metals, Philos. Mag. A 56 (1) (1987) 15–30. doi:10.1080/01418618708204464.

[59] N. Juslin, B. D. Wirth, Interatomic potentials for simulation of He bubble formation in W, J. Nucl. Mater. 432 (1–3) (2013) 61–66. doi:10.1016/j.jnucmat.2012.07.023.

[60] D. E. Beck, A new interatomic potential function for helium, Mol. Phys. 14 (4) (1968) 311–315. doi:10.1080/00268976800100381.

[61] D. E. Beck, Erratum: A new interatomic potential function for helium, Mol. Phys. 15 (3) (1968) 332. doi:10.1080/00268976800101171.

[62] K. Morishita, R. Sugano, B. D. Wirth, T. Diaz de la Rubia, Thermal stability of helium–vacancy clusters in iron, Nucl. Instrum. Meth. Phys. Res. B 202 (2003) 76–81. doi:10.1016/S0168-583X(02)01832-3.

[63] K. D. Hammond, B. D. Wirth, Erratum: Crystal orientation effects on helium ion depth distributions and adatom formation processes in plasma-facing tungsten [J. Appl. Phys. 116, 143301 (2014)], J. Appl. Phys. 118 (22) (2015) 229901. doi:10.1063/1.4938011.

[64] M. Matsumoto, T. Nishimura, Mersenne twister: A 623-dimensionally equidistributed uniform pseudo-random number generator, ACM Trans. Model. Comput. Simulat. 8 (1) (1998) 3–30. doi:10.1145/272991.272995.

[65] S. Nosé, A unified formulation of the constant temperature molecular-dynamics methods, J. Chem. Phys. 81 (1) (1984) 511–519. doi:10.1063/1.447334.

[66] W. G. Hoover, Canonical dynamics: Equilibrium phase-space distributions, Phys. Rev. A 31 (3) (1985) 1695–1697. doi:10.1103/PhysRevA.31.1695.

[67] G. J. Martyna, M. L. Klein, M. Tuckerman, Nosé–Hoover chains: The canonical ensemble via continuous dynamics, J. Chem. Phys. 97 (4) (1992) 2635–2643. doi:10.1063/1.463940.

[68] A. Stukowski, Visualization and analysis of atomistic simulation data with OVITO—the Open Visualization Tool, Model. Simulat. Mater. Sci. Eng. 18 (1) (2010) 015012, http://ovito.org/.

[69] J. Li, AtomEye: An efficient atomistic configuration viewer, Model. Simulat. Mater. Sci. Eng. 11 (2003) 173–177, http://li.mit.edu/Archive/Graphics/A/.

[70] S. G. Wang, E. K. Tian, C. W. Lung, Surface energy of arbitrary crystal plane of bcc and fcc metals, J. Phys. Chem. Solid 61 (8) (2000) 1295–1300. doi:10.1016/S0022-3697(99)00415-1.

[71] S. P. Chen, Theoretical studies of ultrathin film-induced faceting on W(111) surfaces, Surf. Sci. 274 (3) (1992) L619–L626. doi:10.1016/0039-6028(92)90835-T.

[72] J. R. Smith, A. Banerjea, New approach to calculation of total energies of solids with defects: Surface-energy anisotropies, Phys. Rev. Lett. 59 (21) (1987) 2451–2454. doi:10.1103/PhysRevLett.59.2451.

[73] F. R. de Boer, R. Boom, W. C. M. Mattens, A. R. Miedema, A. K. Niessen, Cohesion in Metals: Transition Metal Alloys, North Holland, Amsterdam, 1989.

[74] L. Sandoval, D. Perez, B. P. Uberuaga, A. F. Voter, Growth rate effects on the formation of dislocation loops around deep helium bubbles in tungsten, Fusion Sci. Tech. 71 (1) (2017) 1–6. doi:10.13182/FST16-116.

[75] S. Blondel, K. D. Hammond, L. Hu, D. Maroudas, B. D. Wirth, Modeling helium segregation to the surfaces of plasma-exposed tungsten as a function of temperature and surface orientation, Fusion Sci. Tech. 71 (1) (2017) 22–35. doi:10.13182/FST16-112.

[76] B. D. Wirth, K. D. Hammond, S. Krasheninnikov, D. Maroudas, Challenges and opportunities of modeling plasma surface interactions in tungsten using high performance computing, J. Nucl. Mater. 463 (2015) 30–38. doi:10.1016/j.jnucmat.2014.11.072.

[77] J. J. Billings, D. ~~Bernhold~~Bernholdt, S. Blondel, et al., Xolotl: Plasma–surface interactions, http://sourceforge.net/projects/xolotl-psi/ (2012).

[78] L. Hu, K. D. Hammond, B. D. Wirth, D. Maroudas, Dynamics of small mobile helium clusters near a symmetric tilt grain boundary of plasma-exposed tungsten, Fusion Sci. Tech. 71 (1) (2017) 36–51. doi:10.13182/FST16-105.

[79] S. Blondel, D. E. Bernholdt, K. D. Hammond, L. Hu, D. Maroudas, B. D. Wirth, Benchmarks and tests of a multidimensional cluster dynamics model of helium implantation in tungsten, Fusion Sci. Tech. 71 (1) (2017) 84–92. doi:10.13182/FST16-109.

[80] T. J. Petty, M. J. Baldwin, M. I. Hasan, R. P. Doerner, J. W. Bradley, Tungsten 'fuzz' growth re-examined: The dependence on ion fluence in non-erosive and erosive helium plasma, Nucl. Fusion 55 (9) (2015) 093033. doi:10.1088/0029-5515/55/9/093033.

[81] K. D. Hammond, F. Ferroni, B. D. Wirth, Simulation of helium behavior near sub-surface prismatic dislocation loops in tungsten, Fusion Sci. Tech. 71 (1) (2017) 7–21. doi:10.13182/FST16-110.

Table Captions

Table 1: Lattice parameter (a), reflection coefficient (r; from Ref. 53), fluxes (excluding and including ions that reflect off the surface), size of the simulation, and crystallographic directions corresponding to the Cartesian unit vectors for each simulation.

Surface	(0 0 1)	(0 1 1)	(1 1 1)	(2 1 1)
a (nm)	0.31774	0.31770	0.31805	0.31785
r	0.711	0.707	0.494	0.585
Γ_{nominal} ($\text{m}^{-2}\,\text{s}^{-1}$)	3.968×10^{25}	3.959×10^{25}	4.017×10^{25}	4.009×10^{25}
Γ_{actual} ($\text{m}^{-2}\,\text{s}^{-1}$)	1.37×10^{26}	1.35×10^{26}	7.94×10^{25}	9.66×10^{25}
W block (nm)	$50.20 \times 50.20 \times 25.42$	$50.32 \times 50.20 \times 25.16$	$49.86 \times 49.43 \times 21.48$[a]	$49.55 \times 50.34 \times 24.91$
W atoms[b]	4019204	399296	2486400[c]	3890880
$\hat{e}_x$	[1 0 0]	$\frac{1}{\sqrt{2}}[0\,\bar{1}\,1]$	$\frac{1}{\sqrt{6}}[\bar{1}\,\bar{1}\,2]$	$\frac{1}{\sqrt{3}}[1\,\bar{1}\,\bar{1}]$
$\hat{e}_y$	[0 1 0]	[1 0 0]	$\frac{1}{\sqrt{2}}[1\,\bar{1}\,0]$	$\frac{1}{\sqrt{2}}[0\,1\,\bar{1}]$
$\hat{e}_z$	[0 0 1]	$\frac{1}{\sqrt{2}}[0\,1\,1]$	$\frac{1}{\sqrt{3}}[1\,1\,1]$	$\frac{1}{\sqrt{6}}[2\,1\,1]$

[a] The (1 1 1) simulation started with a block that was 15.98 nm deep. This was increased to 21.48 nm after approximately 150 ns, as the initial depth was deemed too shallow.

[b] This indicates the number of atoms in the simulation just before the first helium atom is implanted.

[c] This was increased to 3338880 after 150 ns

Table 2: Surface tensions (J m^{-2}) for several surface orientations, both from the potential used in this work (EAM; Ref. 56), from other theoretical predictions, and from experimental data, as indicated.

Surface	EAM ([56])	Other theory	Experiment
{1 1 0}	2.58	2.9975 [70]	2.683 [71]
		3.330 [72]	
{3 2 0}	2.84	3.4678 [70]	
{1 0 0}	2.93	4.0246 [70]	3.252 [71]
		5.880 [72]	
{2 1 0}	2.95	3.6957 [70]	
{3 2 1}	2.96	3.3989 [70]	
{3 1 0}	3.03	3.8859 [70]	
{2 1 1}	3.05	3.4614 [70]	3.224 [73]
{2 2 1}	3.12	3.5327 [70]	
{3 1 1}	3.14	3.7689 [70]	
{1 1 1}	3.30	3.6713 [70]	3.510 [73]

Figure Captions

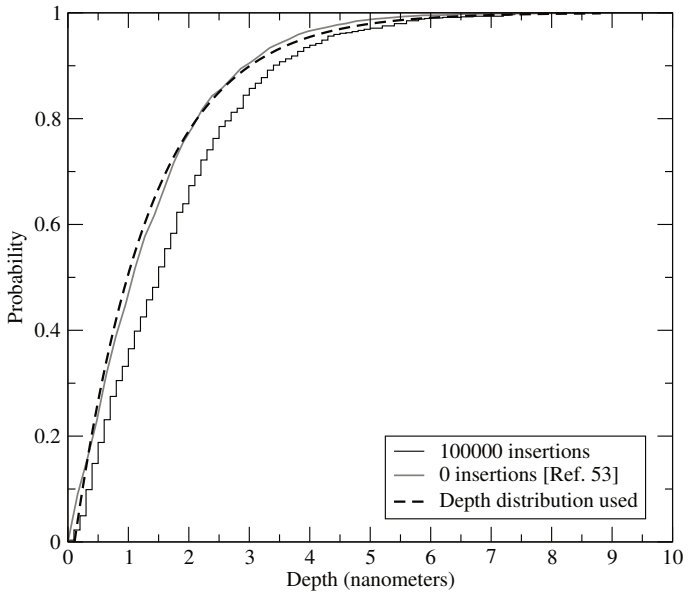

Figure 1: Depth distribution of 100 eV helium atoms after direct bombardment of the W(0 1 1) surface (ignoring reflected atoms). The thick black line shows the distribution used in the simulations, which is an approximation to the initial depth distribution (gray) from our previous work [53]. The stair-step profile shows a similar depth distribution for bombardments on a W(0 1 1) surface after 1.0 μs of helium insertions at a flux of 1.35×10^{26} m^{-2} s^{-1}; the starting configuration for such bombardments is the bottom group of images in Figure 3. Nearly two thirds of helium atoms in these simulations ended up far away from helium bubbles.

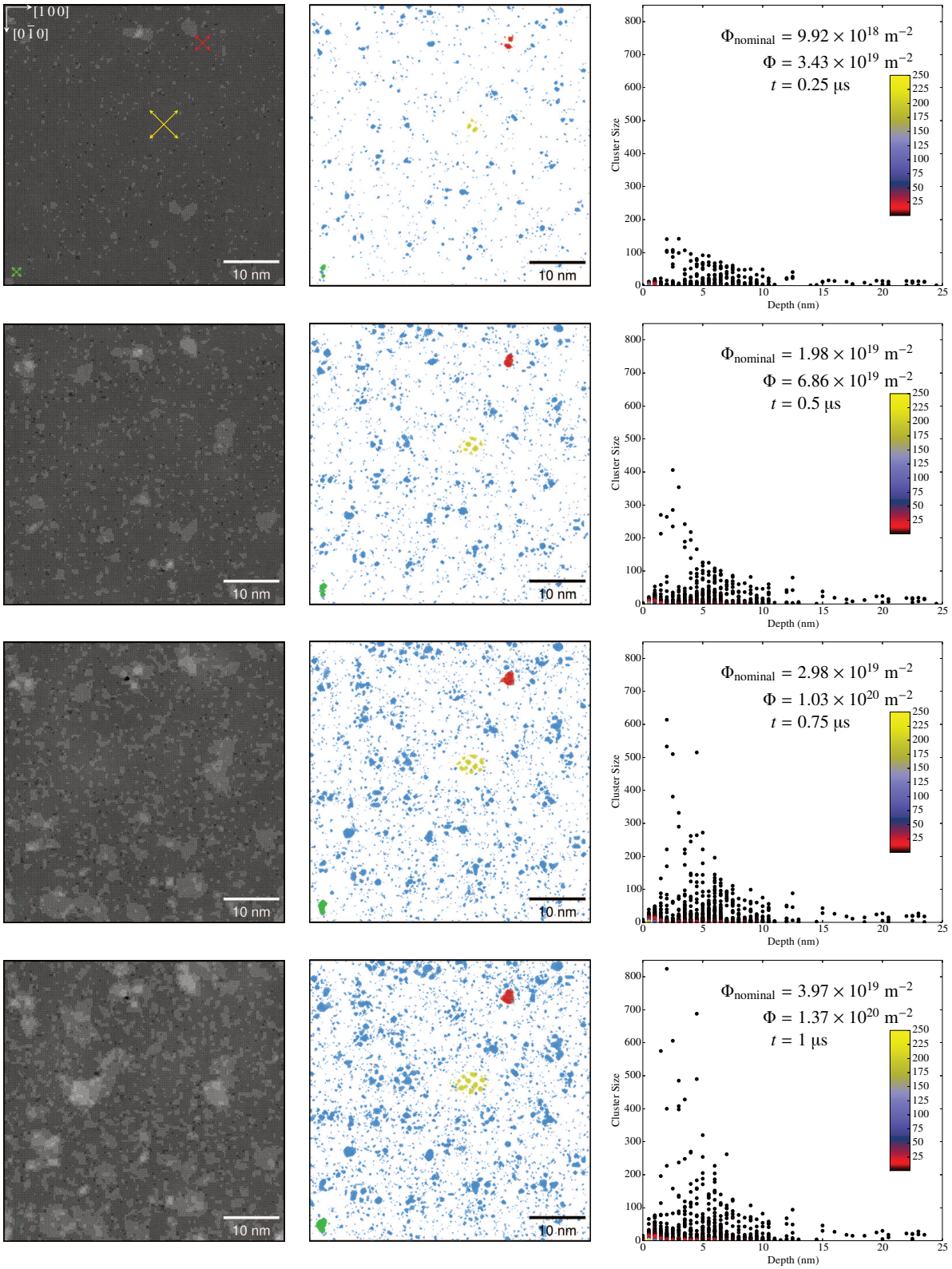

Figure 2: Surface evolution of a W(0 0 1) surface under a nominal flux of 3.97×10^{25} m^{-2} s^{-1}(actual flux $\Gamma = 1.37 \times 10^{26}$ m^{-2} s^{-1}, including reflections) over the course of the first microsecond of time shown through the structural features of a sequence of MD-generated configurations after 0.25, 0.5, 0.75, and 1.0 µs. The left-hand panels show the tungsten surface, tinted according to height above the original surface. The center panels show the same view with tungsten atoms made invisible; three regions of bubbles are highlighted in red, yellow, and green so the bubbles' growth can be readily discerned. The red and green bubbles are both instantaneous configurations of a single larger bubble formed by the coalescence of smaller ones, while the yellow is a cluster of bubbles, each individually immobilized by vacancies, that are in the same region of the metal. The arrows in the left-hand panel show the center of each bubble and its ⟨1 1 1⟩ slip directions, with arrow lengths proportional to the depth of the bubble. The right-hand panels show the helium cluster size distribution as a function of depth; the number of clusters of each size is indicated by color.

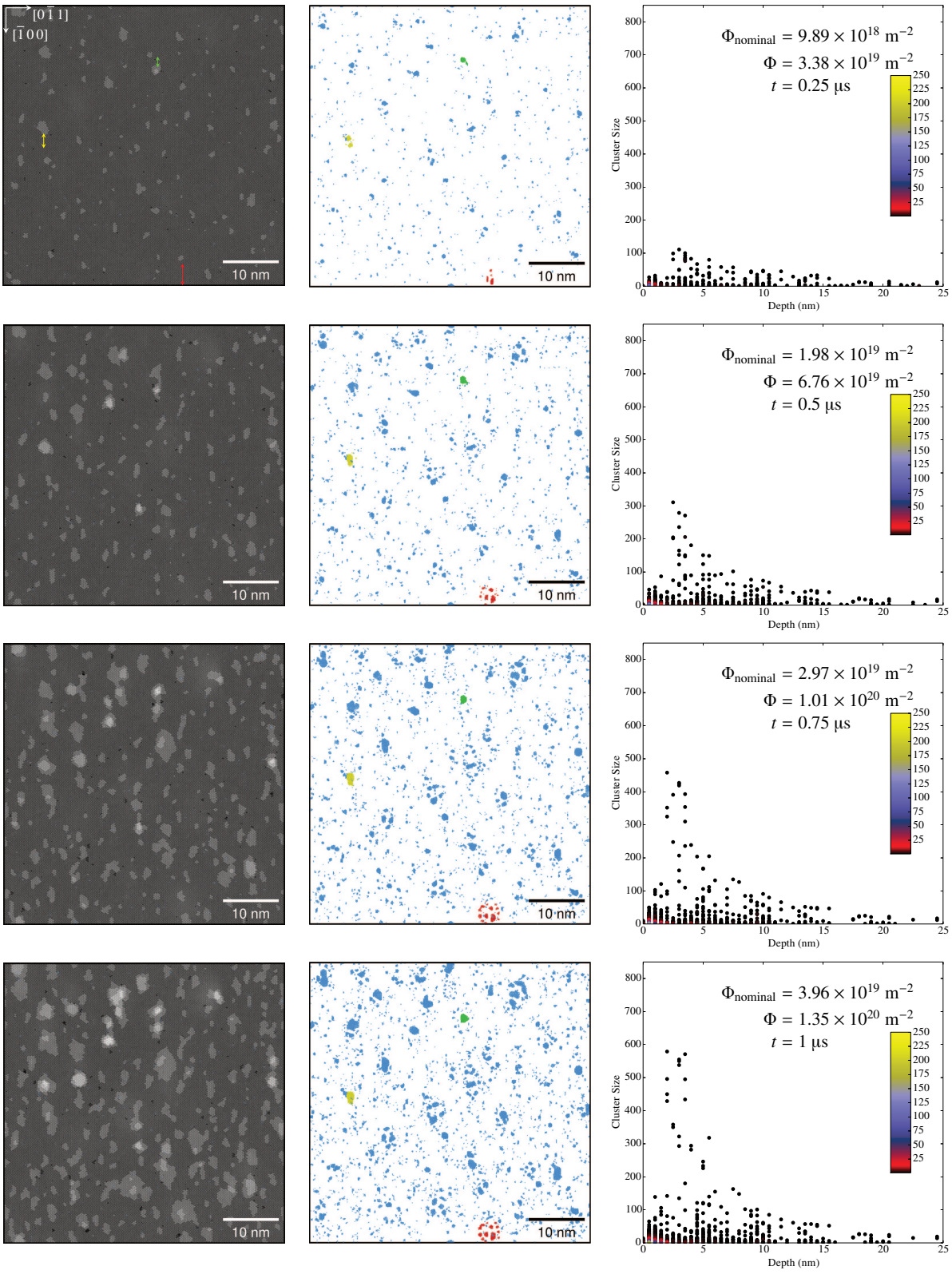

Figure 3: Surface evolution of a W(0 1 1) surface under a nominal flux of 3.97×10^{25} m^{-2} s^{-1}(actual flux $\Gamma = 1.35 \times 10^{26}$ m^{-2} s^{-1}, including reflections) over the course of the first microsecond of time, analogous to that in Figure 2. The much more "orderly" formation of features on this surface is due to the higher mobility of adatoms on {0 1 1} surfaces compared to that on {0 0 1} surfaces with this potential. All three highlighted bubbles (and bubble clusters) are directly responsible for surface features immediately above or below them (i.e., in the ±[1 0 0] directions, resulting from dislocation motion from the bubble in the [1 1 1] and [$\bar{1}$ 1 1] directions, which are drawn with arrows of length proportional to the respective bubble depths).

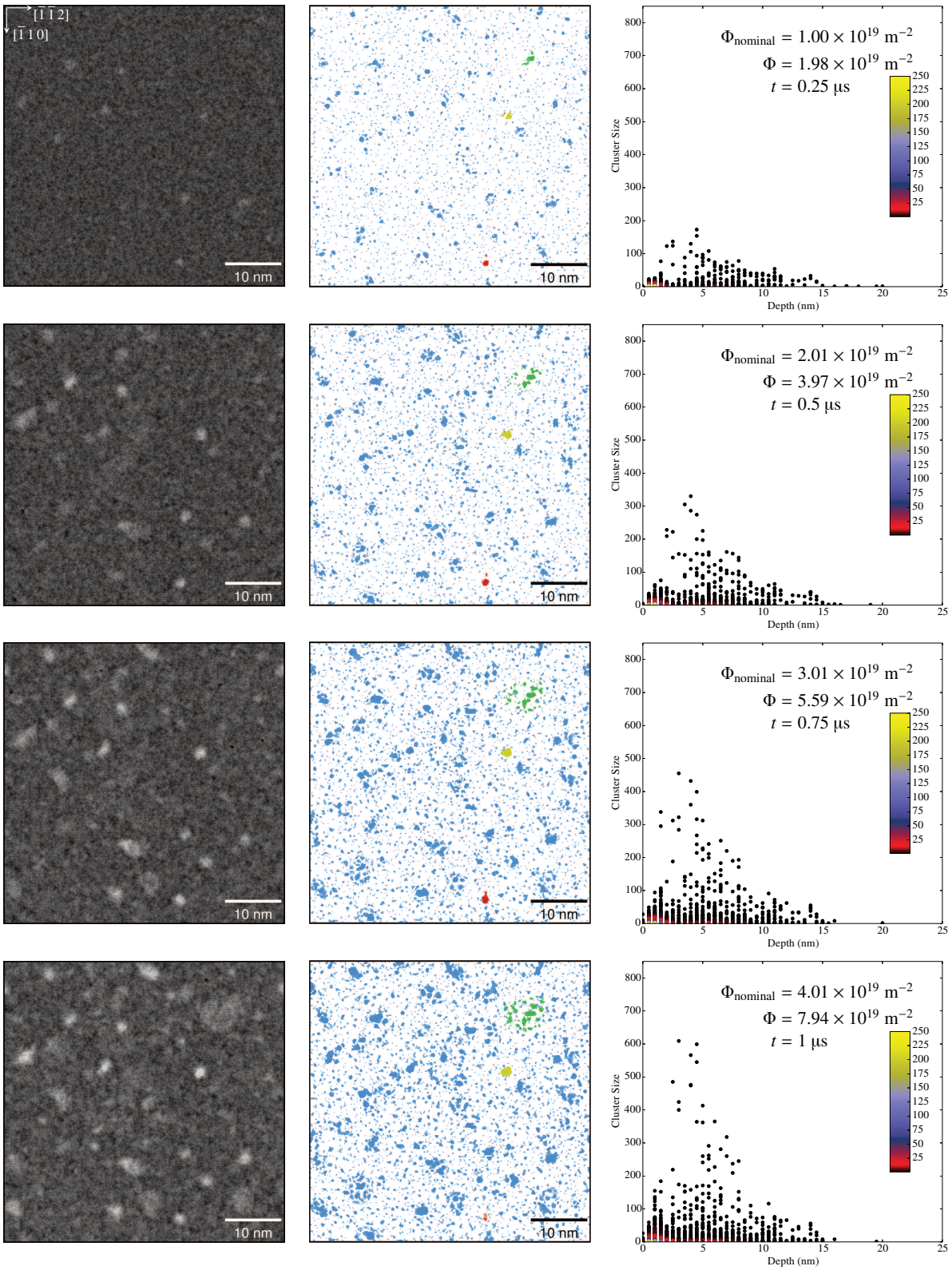

Figure 4: Surface evolution of a W(1 1 1) surface under a nominal flux of 4.02×10^{25} m^{-2} s^{-1}(actual flux $\Gamma = 7.94 \times 10^{25}$ m^{-2} s^{-1}, including reflections) over the course of the first microsecond of time, analogous to that in Figures 2 and 3. In this orientation, the Burgers vectors of potential dislocation loops near bubbles are normal to the surface, creating surface defects (adatom "islands") directly above the bubble. The resulting surface features "pile up," yielding dome-like structures. The yellow cluster is a single bubble that creates such a dome. The green cluster is a group of bubbles that collectively form the raised spot in the upper right, while the red bubble actually bursts at approximately 821 ns; the resulting rupture heals and the bubble partially re-fills.

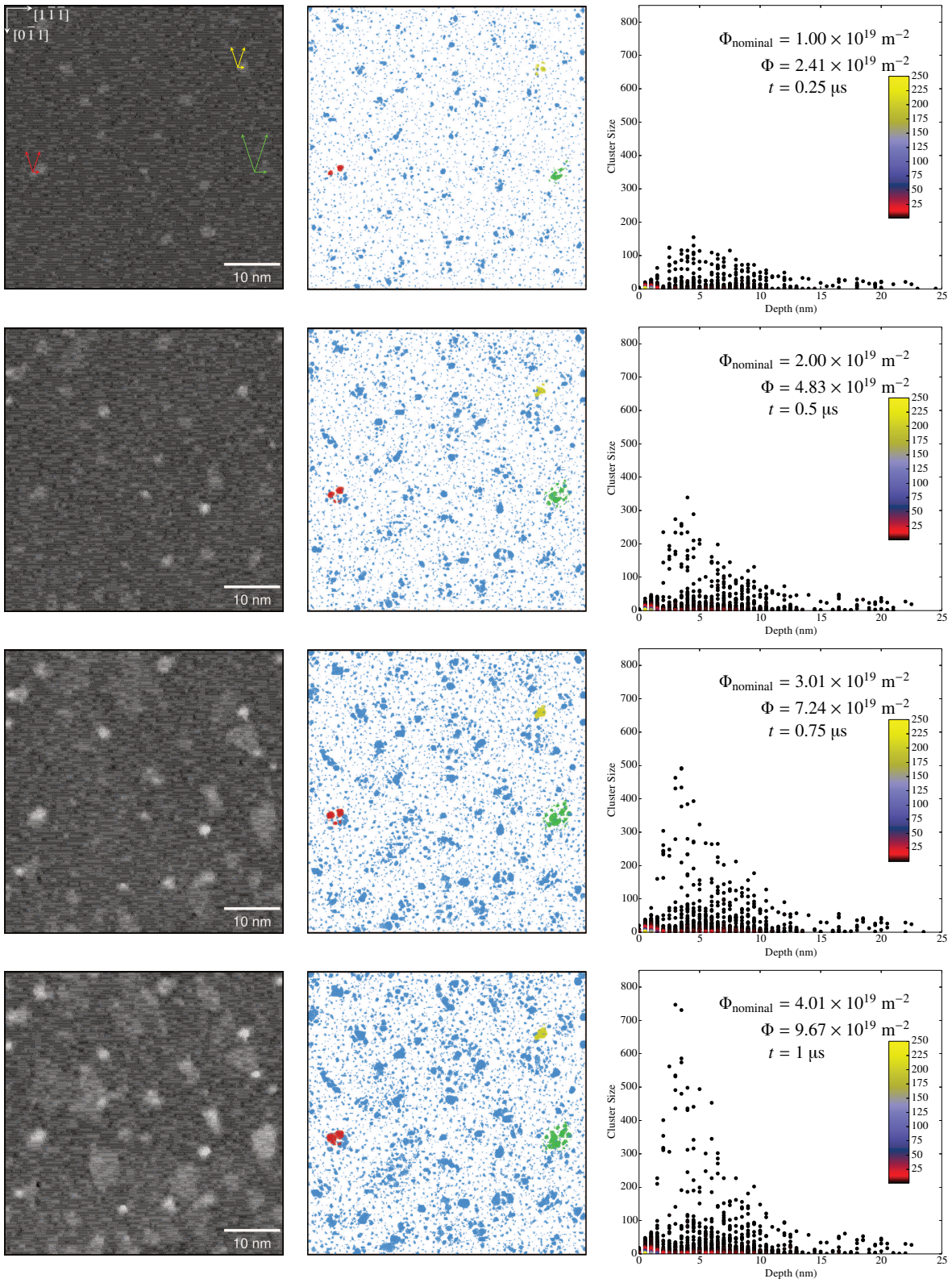

Figure 5: Surface evolution of a W(2 1 1) surface under a nominal flux of 4.01×10^{25} m^{-2} s^{-1}(actual flux $\Gamma = 9.66 \times 10^{25}$ m^{-2} s^{-1}, including reflections) over the course of the first microsecond of time, analogous to that in Figures 2–4. In this orientation, diffusion of adatoms is rapid in the left/right directions (i.e., the $[1\,\bar{1}\,\bar{1}]$ and $[\bar{1}\,1\,1]$ crystallographic directions), but much slower in the up/down directions (i.e., the $[0\,\bar{1}\,1]$ and $[0\,1\,\bar{1}]$ directions). This causes "rows" of atoms to form on the surface. However, the primary mechanism of damage is similar to that on the (1 1 1) surface due to the fact that the ⟨1 1 1⟩ directions are only about 19.5° from being normal to the surface.

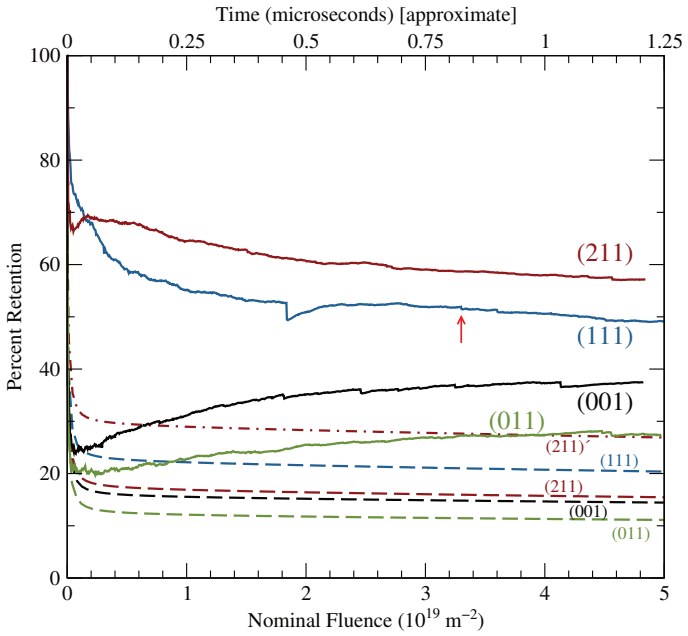

Figure 6: Helium retention (percentage of implanted helium that remains in the tungsten at that instant) as a function of fluence and time for the four surface orientations shown over the first 1.25 μs of plasma exposure. Also shown (dashed lines) are estimates from Xolotl [77] of what the retention *would* be in the absence of bubble formation (trap mutation/bubble nucleation); the "drift" terms [34, 35, 54] are still present. The sharp reduction in the case of the (1 1 1) surface at 0.46 μs is actually a coincidental release of several small, near-surface bubbles rather than a bubble-bursting event involving one larger bubble. The smaller abrupt decreases in the case of the (0 0 1) surface, for example, correspond to individual small bubbles bursting. The arrow indicates the bursting of the bubble as depicted in red in Figure 4 for the case of the (1 1 1) surface.

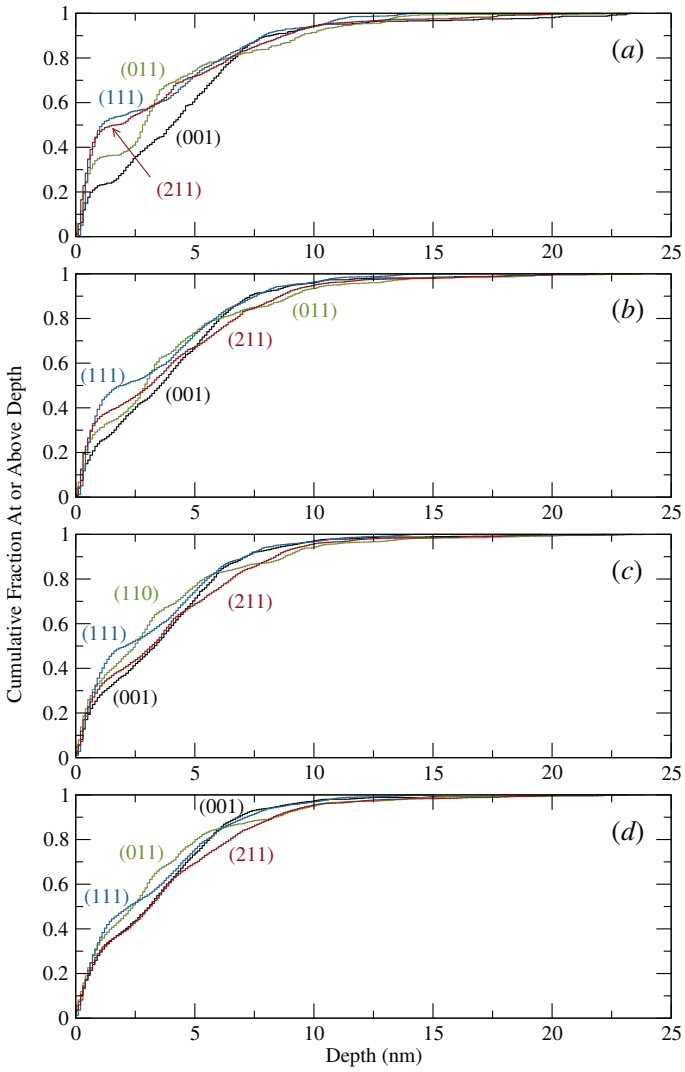

Figure 7: Distribution of helium as accumulated after implantation into tungsten for four different surface orientations at (*a*) 0.25 μs, (*b*) 0.50 μs, (*c*) 0.75 μs, and (*d*) 1.00 μs of helium implantation. Note that the primary "features" of the depth distribution are still developing at 0.25 μs, but have largely reached steady-state by 0.5 μs. Note also that orientation plays much less of a role at long times (> 100 ns) than it does at short times (cf. Maroudas et al. [54], Fig. 7a).

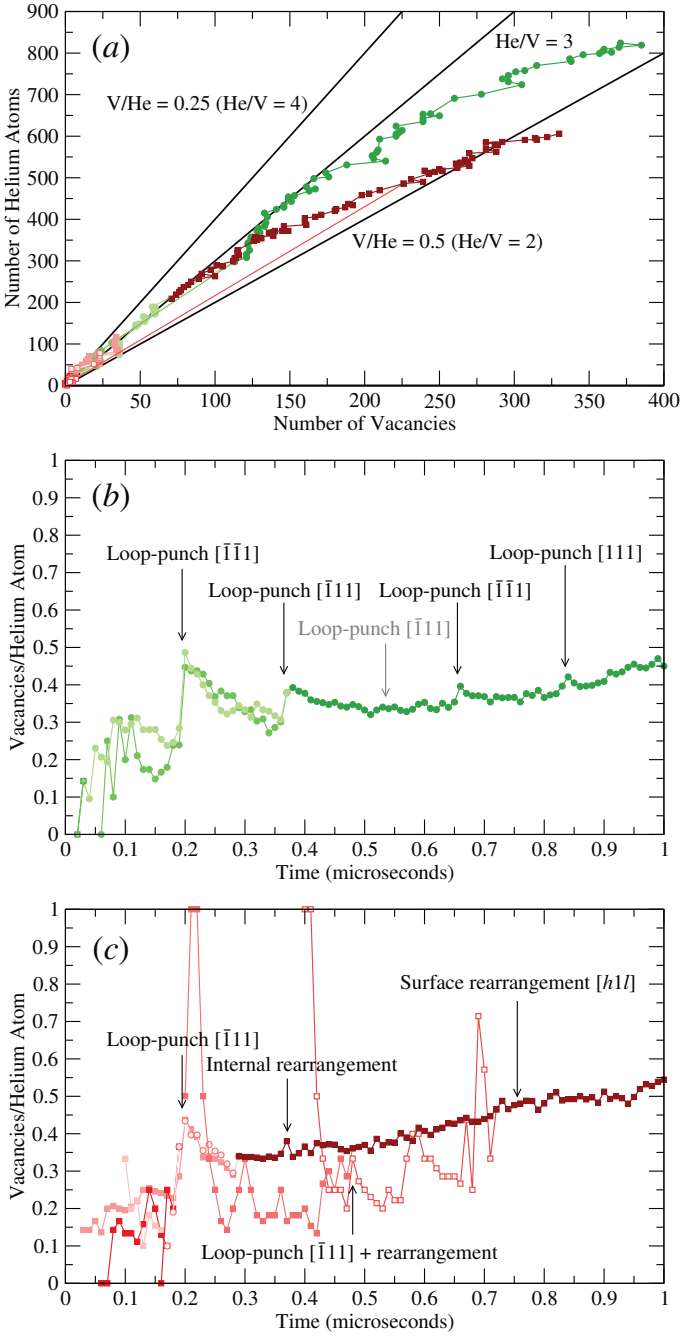

Figure 8: (*a*) Helium content as a function of bubble size (i.e., vacancies per bubble); and evolution of vacancy-to-helium ratio (V/He) for the green (*b*) and red (*c*) bubbles in Figure 2, corresponding to a (0 0 1) surface orientation. Abrupt changes in the V/He ratio are often, but not always, linked to loop-punching events (manifesting as the sudden appearance of adatom islands above the bubble, emanating from it in ⟨1 1 1⟩ directions).

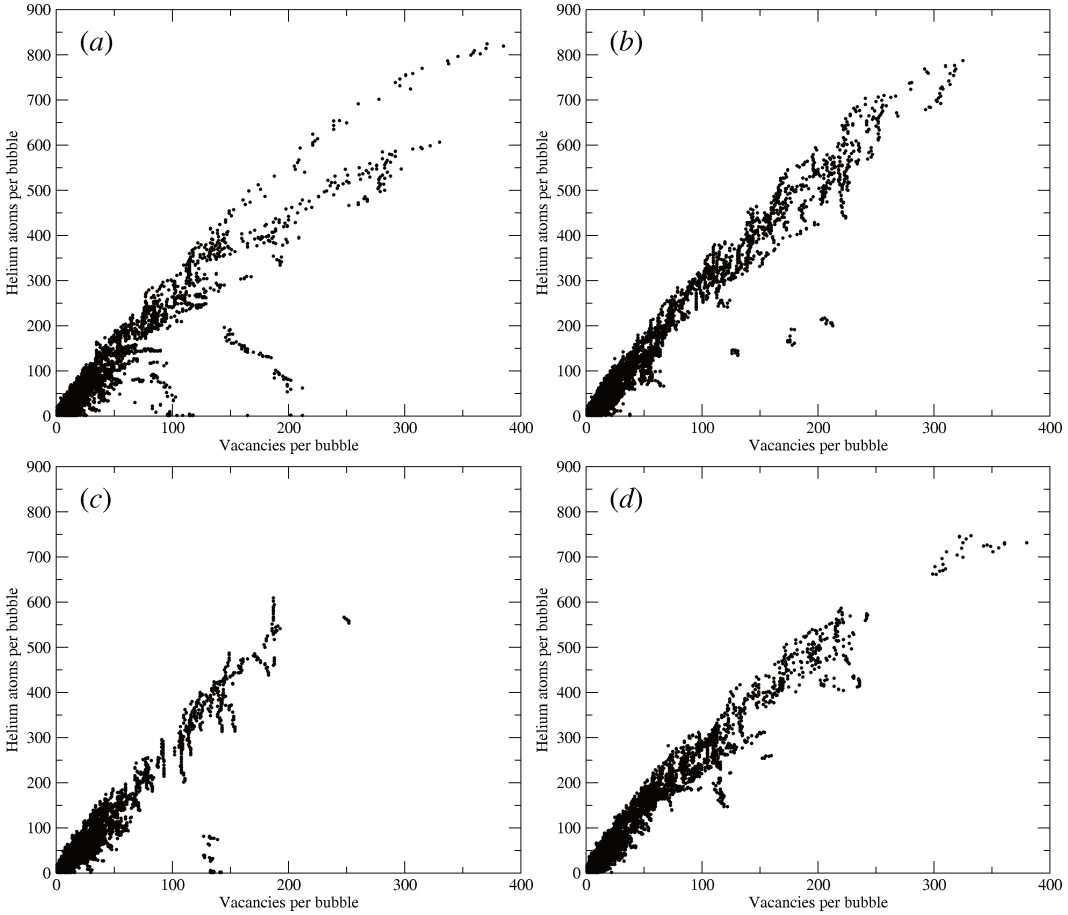

Figure 9: Bubble size/density data (number of helium atoms per bubble as a function of the number of vacancies per bubble) for (*a*) (0 0 1), (*b*) (0 1 1), (*c*) (1 1 1), and (*d*) (2 1 1) surface orientations for bubbles within 4 nm of the original surface, for the period 0–1 μs. Each point represents a bubble present at a particular instant in time during the simulations, sampled every 10 ns for 1 μs, so many of the dots correspond to the same bubble at different times.

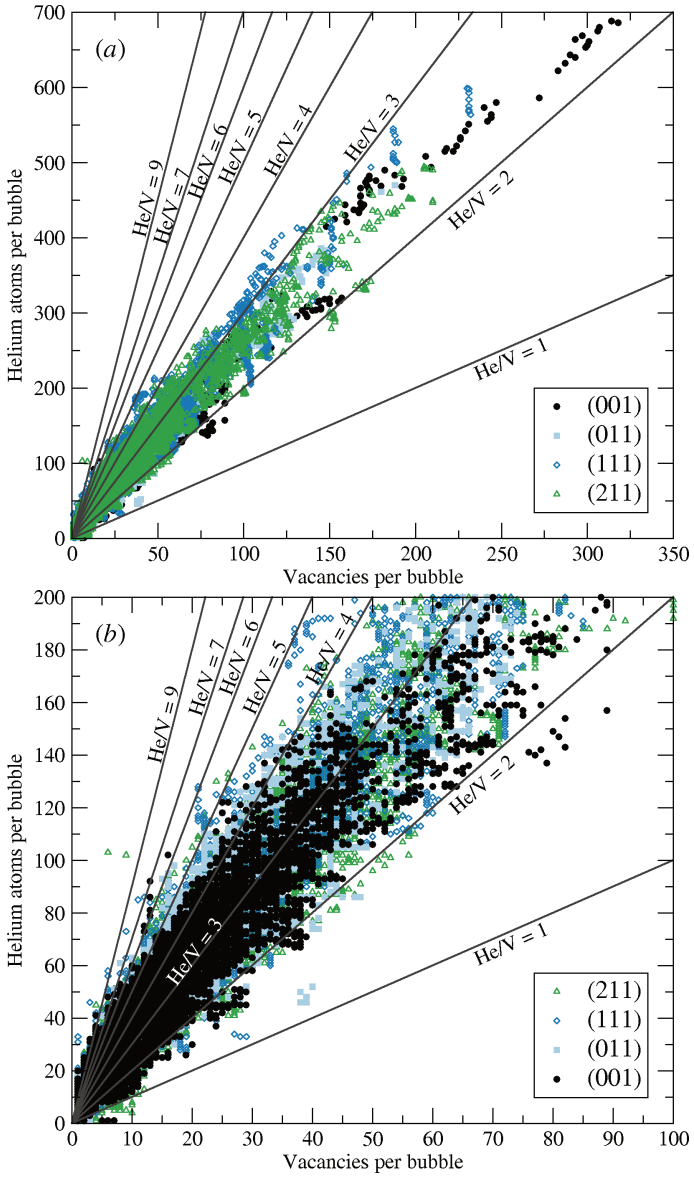

Figure 10: (*a*) Bubble size/density data (number of helium atoms per bubble as a function of the number of vacancies per bubble) for all four surface orientations for bubbles more than 4 nm from the original surface (i.e., the location of the surface prior to plasma exposure). Lines representing different He/V ratios are shown for reference. (*b*) The same plot as in (*a*) over a different domain of vacancies per bubble and the data series in reverse order (bottom to top) for better clarity regarding what the bounds are for each surface. Each point represents a bubble present at a particular instant in time, sampled every 10 ns for 1 μs.

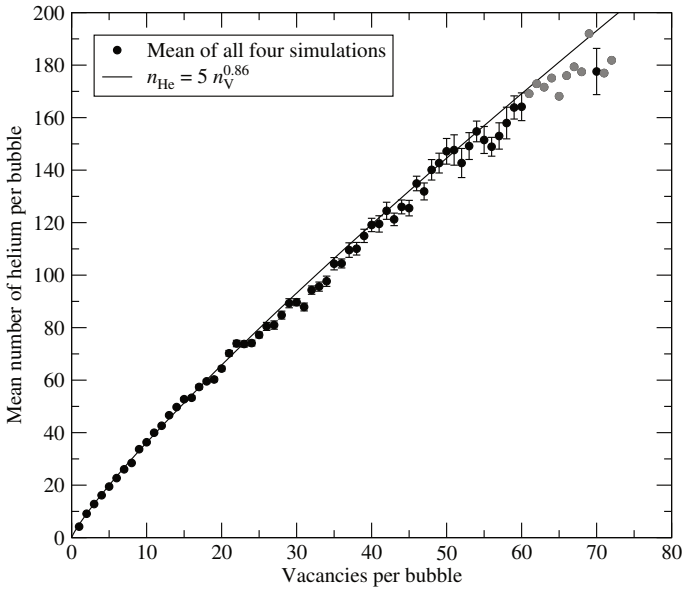

Figure 11: Mean number of helium atoms in a bubble of a given size, as denoted by the number of vacancies the bubble occupies, for bubbles more than 4 nm beneath the surface. Error bars are 95% confidence intervals. For clarity, all "averages" that are based on only one point are denoted by solid gray rather than black circles.

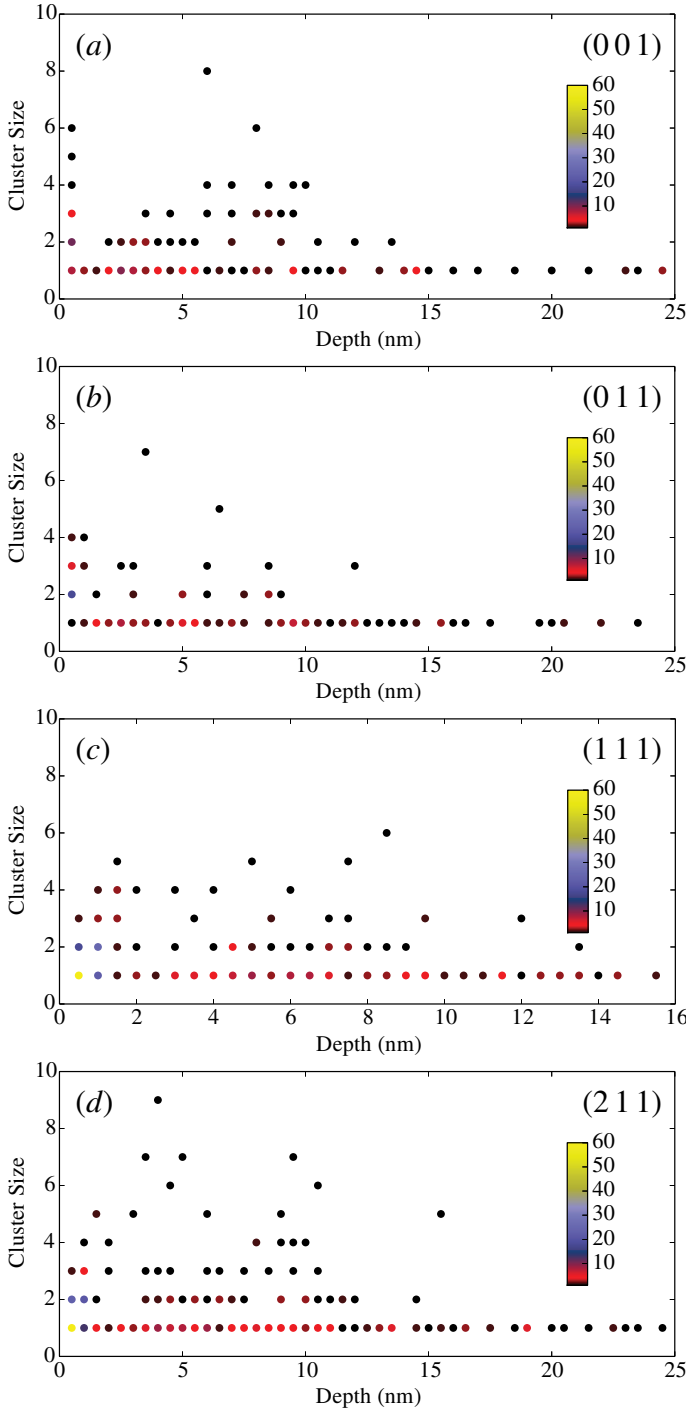

Figure 12: Cluster size distributions for each of the four surface orientations after only 10 ns of simulation time ($\Phi_{\text{nominal}} \approx 4.0 \times 10^{17}$ m^{-2}). The colors indicate the number of clusters of a given size and depth. Note the presence—in all four cases—of helium clusters at or near the bottom of the simulation box, which is the rightmost point of the range of the abscissa in all four plots. This indicates that "deep" helium diffusion is not impeded strongly early-on in the simulation, allowing for the possibility of deep-seated helium bubbles despite the "protective layer" of helium bubbles that forms rapidly near the surface in the first 100 ns or so.